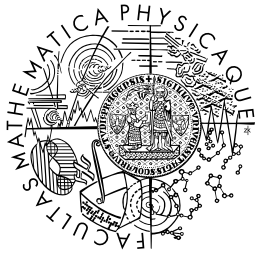

FACULTY
OF MATHEMATICS
AND PHYSICS
Charles University

SUMMARY OF DOCTORAL THESIS

Jan Premus

Joint inverse modeling of coseismic and postseismic slip of the 2014 South Napa, California, earthquake

Department of Geophysics

Supervisor of the doctoral thesis: prof. František Gallovič

Study programme: Physics

Study branch: Physics of the Earth and Planets

Prague 2023

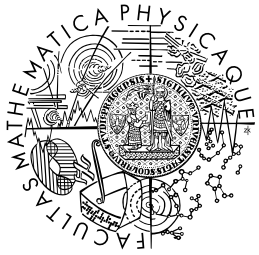

FACULTY
OF MATHEMATICS
AND PHYSICS
Charles University

AUTOREFERÁT DIZERTAČNÍ PRÁCE

Jan Premus

Sdružené inverzní modelování koseismického a postseismického skluzu kalifornského zemětřesení South Napa 2014

Department of Geophysics

Vedoucí dizertační práce: prof. František Gallovič
Studijní program: Fyzika
Studijní obor: Fyzika Země a Planet

Praha 2023

Dizertace byla vypracována na základě výsledků získaných v letech 2019-2022 během doktorandského studia na Katedře geofyziky MFF UK.

Dizertant:
Mgr. Jan Premus
Katedra geofyziky MFF UK
V Holešovičkách 2, 180 00 Praha 8

Školitel:
prof. František Gallovič
Katedra geofyziky MFF UK
V Holešovičkách 2, 180 00 Praha 8

Oponenti:
Elisa Tinti Ph.D.
Assoc. Prof.
Istituto Nazionale di Geofisica e Vulcanologia
Via di Vigna Murata, 605, 00143 Rome

RNDr. Jan Burjánek, PhD.
Geofyzikální ústav Akademie věd, v. v. i.
Boční II/1401, 141 31 Praha 4

Předsedkyně oborové rady:
doc. RNDr. Hana Čížková, Ph.D.
Katedra geofyziky MFF UK
V Holešovičkách 2, 180 00 Praha 8

Obhajoba dizertace se koná dne 22.2.2023 v 13:00 hodin před komisí pro obhajoby dizertačních prací v oboru Fyzika Země a planet v budově MFF UK, Ke Karlovu 3, Praha 2 v místnosti M252.
S dizertací je možno se seznámit v PGS MFF UK, Ke Karlovu 3, Praha 2.

Contents

1. Introduction

Tectonic faults occur in the Earth's crust as a brittle response to the elastic accumulation of stress, usually at boundaries between tectonic plates. Accumulated stress releases in the form of slip — the mutual movement of both sides of the fault.

Slip can unfold continuously over many decades on the so-called creeping segments of the faults [Harris, 2017]. On other parts of the faults, slip takes place over a wide range of temporal scales, from sub-second to minute scale of seismic slip during earthquakes, up to months and years of aseismic slip [Marone et al., 1991, Perfettini and Avouac, 2004]. The concept of the tectonic loading of stress, and its release through quasiperiodic earthquakes and aseismic slip is known as the seismic cycle [Perfettini et al., 2003, Hillers et al., 2006, Perfettini and Avouac, 2014, Bunichiro et al., 2019].

Faulting is prominent in the Earth's crust, constrained roughly to maximum depths of 20–50 km as high temperatures at larger depths preclude brittle fracture in favor of viscoelasticity and plasticity [Scholz, 1998]. Exceptions are the intermediate and deep earthquakes that can occur in the colder material of subducted slabs at depths of up to 700 km [Frohlich, 2006].

As the stress preferably releases on preexisting faults, the occurrence of slip is considered to be a more frictional than fracturing phenomenon [Scholz, 1998]. Fracture mechanics plays a supporting role mostly during the extension of the existing faults [Cowie and Scholz, 1992], the creation of new ones, or the damage of surrounding material [Yamashita, 2000, Okubo et al., 2019]. Two empirical models of friction are prominent in the seismological community. Slip-weakening friction laws [Andrews, 1976] describe the basic behavior of friction decrease from static to dynamic value during the slipping and is thus suitable for earthquake modeling. It cannot be used to explain the behavior of aseismic slip, or strength recovery during the interseismic phase. Rate-and-state friction models [Dieterich, 1972, Ruina, 1983] encompass these phenomena, with an elegant explanation of the seismic and aseismic slip dichotomy through velocity-weakening and velocity-strengthening frictional rheology. Quasiperiodic occurrence of earthquakes has an analog in simple stick-slip models [Brace and Byerlee, 1966] where the string-pulled object on the velocity-weakening contact alternates between periods of fast slip and longer periods of movement cessation.

Experimental research of frictional, fracture, or other mechanisms is limited by the spatial scale achievable in laboratory [Viesca and Garagash, 2015]. The typical size of samples in frictional experiments is measured in centimeters to meters [Dieterich, 1979], while the faults in nature span up to tens to hundreds of kilometers. Nevertheless, laboratory experiments led to important advancements, such as the discovery of contact fast-weakening due to flash-heating [Di Toro et al., 2004], which is thought to preclude the complete melting of fault contacts during the earthquake, observed only rarely [Rice, 2006].

Earthquake science is becoming increasingly data-rich, given the increasing number of installed seismic and geodetic stations [Storchak et al., 2020] and the advent of emerging technologies, such as remote sensing [Lohman et al., 2002] or distributed acoustic sensing [Daley et al., 2013]. These observations are limited

to the surface effects of burried fault phenomena in the form of ground motions or surface displacements. Direct measurements on active faults are usually inaccessible, with only a few technically difficult exceptions, such as drilling into the fault [Fulton et al., 2019]. Consequent difficulties in discerning relative importance of various physical phenomena is the substantive reason for earthquake science remaining relatively model-poor [Lapusta et al., 2019].

Physics-based dynamic rupture modeling provides a bridge between the small scales of laboratory experiments and the large scales of earthquake observations. It assimilates the results of experimental studies into complex computer simulations, where the slip propagates on pre-existing faults, governed by internal stresses and friction on the fault. This facilitates parametric numerical experiments [e.g., Kaneko et al., 2008, Gabriel et al., 2012, Bai and Ampuero, 2017], or modeling of specific events [e.g., Peyrat et al., 2001, Ando and Kaneko, 2018, Gallovič et al., 2020, Tinti et al., 2021].

Dynamic rupture simulations have been undergoing rapid development in the past decades, starting with finite difference (FD) [e.g., Andrews, 1976, Madariaga, 1976] and boundary integral [e.g., Burridge, 1969] methods. Later, finite element [e.g., Barall, 2006], spectral element [e.g., Kaneko et al., 2008], and discontinuous Galerkin[de la Puente et al., 2009] methods were developed.

Empowered by supercomputing [e.g., Heinecke et al., 2014], 3D dynamic rupture earthquake simulation software has reached the capability of accounting for increasingly complex geometrical [e.g., Ulrich et al., 2019] and physical [e.g., Roten et al., 2014]) modeling components in high-resolution single-event scenarios. Yet, the computational cost of such dynamic rupture models hinders applications requiring a large number of simulations.

Fitting data that carry information about the faulting process is a strongly nonlinear problem termed dynamic earthquake source inversion [Fukuyama and Mikumo, 1993]. For a specific earthquake, the dynamic model is parametrized by the spatial distribution of initial stress and frictional parameters, collectively referred to as dynamic parameters. These parameters are then optimized to minimize the misfit between synthetic and real data. Only a handful of earthquake dynamic inversions were performed [Gallovič et al., 2019a], all employing slip-weakening friction. The employment of more realistic rate-and-state friction laws in dynamic source inversions is yet to be properly explored.

1.0.1 2014, South Napa Earthquake

The 24 August 2014 Mw 6.0 South Napa, California earthquake has a particularly well-documented abundance of coseismic and postseismic slip, making it a good target for dynamic source inversion. It ruptured one of the recently mapped branches of the West Napa fault [Wesling and Hanson, 2008]. The earthquake's right-lateral strike-slip mechanism is consistent with the orientation of this fault. The shallow part of the fault (<3 km depth) span two lithological units [Graymer et al., 2005]: The northern half is positioned on the contact between Cretaceous rocks (sandstone, melange, etc.) from the Franciscan Complex and Cenozoic sediments, while the southern half of the fault goes below the Napa River and is embedded in a layer of Quaternary sediments [Graymer et al., 2005, Floyd et al., 2016, Langenheim et al., 2010] whose thickness increases in the southward

direction from 1.5 km to more than 2 km (see Figure 3.1a for the fault position with respect to the regional geology).

The 2014 South Napa earthquake is well studied, including measurements of surface slip and afterslip over the whole length of the rupture [Lienkaemper et al., 2016, DeLong et al., 2016]. Kinematic studies of coseismic and postseismic slip [Floyd et al., 2016, Dreger et al., 2015, Ji et al., 2015, Melgar et al., 2015] agree on the main source characteristics. The rupture nucleated at 10 km depth and propagated up-dip and northward for 8 to 10 s along a 13-km distance, generating strong seismic waves amplified toward the north due to the source directivity and a sedimentary basin [Ji et al., 2015]. The event produced a 12-km-long surface rupture and rapid shallow afterslip [Floyd et al., 2016, Brooks et al., 2017]. It was also followed by approximately 1000 aftershocks that occurred mostly below the coseismic rupture [Hardebeck and Shelly, 2016]. While most of the shallow coseismic slip was concentrated in the northern half of the rupture, an unusually large shallow afterslip occurred on the southern half, starting 3 hours after the earthquake and continuing over the next several months [Brooks et al., 2017]. This spatial difference in the release of shallow slip has been attributed to spatial variability of either the local geology [Floyd et al., 2016, Brooks et al., 2017] or the coseismic stress changes [Wei et al., 2015].

1.1 Content of the Thesis

This thesis expands the scope of the dynamic inversion beyond the coseismic rupture and perform the first joint physics-based inverse modeling of an earthquake with its afterslip. The 2014 Napa earthquake offers a perfect case study for the new approach due to the wealth of available recordings of both coseismic and postseismic slip that significantly contributed to the released energy and damage caused to human structures.

We utilize a state-of-the-art laboratory-derived rate-and-state friction law with enhanced fast-velocity-weakening representing a unifying physical framework to capture both the co- and postseismic slip. To this aim, we introduce an efficient finite-difference code FD3D_TSN with GPU acceleration. Our Bayesian inverse modeling is constrained by multiple datasets on diverse timescales from seconds (seismograms and coseismic GPS) to months (postseismic GPS and alignment fields across the surface rupture).

In addition, we compare the results with the dynamic inversion of the same earthquake, which employs the slip-weakening friction law. This allows us to make comparisons between the friction models, determine which properties of the dynamic models are affected by the choice of the friction law, and demonstrate the usefulness of the expansion to postseismic modeling even for constraining the coseismic phase.

2. Dynamic and quasidynamic simulations of earthquake rupture

2.1 Method

2.1.1 Friction law

FD3D_TSN features two friction laws: (1) classical slip-weakening law [Ida, 1972, Andrews, 1976] and (2) rate-and-state law with rapid velocity weakening at high slip rates [Ampuero and Ben-Zion, 2008, Beeler et al., 2008], as proposed by Dunham et al. [2011]. Although the numerical implementation of the former is straightforward, the latter needs a specific approach as it is complicated by the need to solve an additional set of two ordinary differential equations at every node along the fault.

The linear slip-weakening friction law [Ida, 1972] is widely used in dynamic rupture simulations. The value of the effective friction coefficient depends only on the slip s:

$$S = \sigma_n f(s). \tag{2.1}$$

We consider the linear slip-weakening relationship in the form introduced by Andrews [1976]:

$$f(s) = \begin{cases} f_s - (f_s - f_d)s/D_c, & \text{if } s < D_c \\ f_d, & \text{if } s \geq D_c, \end{cases} \tag{2.2}$$

where f_s, f_d and D_c are initial model parameters. During the sliding frictional coefficient linearly decreases from the static value f_s to the dynamic value $f_d < f_s$ over a characteristic slip-weakening distance D_c as shown in Figure 2.1.

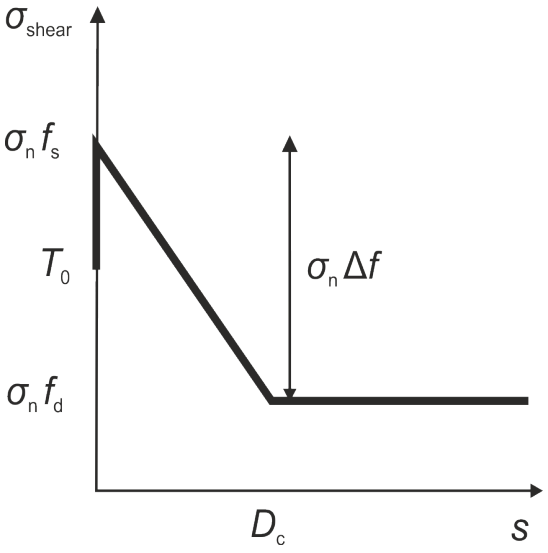

Figure 2.1: Illustrative plot of SW friction, thick black line shows the development of friction with slip.

In our joint inversion, coseismic and postseismic slip are governed by rate-and-state friction with fast-velocity-weakening [Dunham et al., 2011]

$$S = \sigma_n a \, \mathrm{arcsinh}\Big[\frac{\dot{s}}{2\dot{s}_0}\exp\Big(\frac{\psi}{a}\Big)\Big] \tag{2.3}$$

$$\frac{d\psi}{dt} = -\frac{\dot{s}}{L}[\psi - \psi_{SS}] \tag{2.4}$$

$$\psi_{SS} = a \log\Big[\frac{2\dot{s}_0}{\dot{s}} \, \sinh\Big(\frac{f_{SS}}{a}\Big)\Big] \tag{2.5}$$

$$f_{SS} = f_w + \frac{f_{LV} - f_w}{\Big[1 + (\dot{s}/\dot{s}_w)^8\Big]^{1/8}} \tag{2.6}$$

$$f_{LV} = f_0 - (b - a) \log\Big(\frac{\dot{s}}{\dot{s}_0}\Big) \tag{2.7}$$

Equation 2.3 gives a value of friction S for given slip rate $\dot{s}$ and frictional state variable ψ. It is in the regularized form to avoid divergence at zero slip rate [Rice and Ben-Zion, 1996, Lapusta et al., 2000], with only minor difference from the classical formulation for $\dot{s} > 0$ [Ruina, 1983]. The evolution equation (Equation 2.4) for the state variable ψ is the slip law, in which the time derivative of the state variable is proportional to its distance to a steady-state value ψ_{SS} and ratio of $\dot{s}$ and characteristic slip L. The steady-state value is calculated in Equation 2.5 from steady-state friction f_{SS} as an inverse function of Equation 2.3. The steady-state friction is defined by Equation 2.6, where it decreases from low-velocity friction f_{LV} to fully weakened friction f_w with growing slip rate $\dot{s}$, as $\sim 1/\dot{s}$ for $\dot{s} > \dot{s}_w$ due to the fast-velocity-weakening effect, following the flash-heating model [Rice, 2006]. The low-velocity steady-state friction coefficient f_{LV} defined by Equation 2.7 increases or decreases with slip rate $\dot{s}$ following the sign of the difference between the state evolution b and direct effect a coefficients. The difference $(b - a)$ in Equation 2.7 thus distinguishes the velocity-weakening $(b-a > 0)$ and velocity-strengthening $(b-a < 0)$ modes of friction [Scholz, 2012].

2.1.2 Forward problem

We simulate the coseismic rupture with the code FD3D_TSN [Premus et al., 2020]. It uses a fourth-order finite-difference method to solve the 3D elastodynamic equation. The fault boundary condition (friction) is applied on a vertical fault with the traction-at-split-nodes method [Dalguer and Day, 2007]. Free surface conditions are applied using a stress imaging technique [Graves, 1996]. We use perfectly matched layers [Collino and Tsogka, 2001] as absorbing boundary conditions. All computationally expensive routines are GPU-accelerated using OpenACC directives, yielding a speedup by a factor of 10 when comparing single GPU and single CPU runs. Accuracy of the code was tested [Premus et al., 2020] by using community Southern California Earthquake Center/U.S. Geological Survey (SCEC/USGS) benchmarks for both slip-weakening and fast-velocity-weakening friction laws [Harris et al., 2018]. Earthquake nucleation is induced by

a second-long gradual increase of prestress in a circular zone. Synthetic seismograms are obtained by convolving the resulting slip rates with Green's functions precalculated using the Axitra code [Cotton and Coutant, 1997].

Postseismic slip is simulated in a quasidynamic approximation, replacing the inertial term of the elastodynamic equation by a radiation damping on the fault [Rice, 1993]. We use a boundary element approach with a precalculated velocity-stress interaction kernel between fault nodes, assuming a vertical fault in a homogeneous medium [Okada, 1985]. This reduces the problem to a set of ordinary differential equations for displacements and state variables [Perfettini et al., 2003, Gallovič, 2008, Galvez et al., 2021]. We solve it by a Runge-Kutta method of fifth order with variable time steps. This quasidynamic postseismic modeling is used after the maximum slip rate in the finite-difference coseismic simulation falls below 1 mm/s.

2.1.3 Parameterization

The fast-velocity-weakening rate-and-state friction law involves a challenging number of potentially free parameters in the dynamic inversion, increasing the dimension of the model parameter space and increasing computational requirements. These include parameters of the rate-and-state friction a, b, f_0, s_0, and L; additional parameters governing the fast-velocity-weakening effect f_w and s_w; stressing conditions at the fault σ_n and T_0; and initial values s_{ini} and ψ_{ini}. We assume a purely strike-slip fault so that T_0 and s_{ini} are non-zero only in the horizontal direction. All parameters are thus spatially heterogeneous 2D scalar fields across the fault.

We use several relations and assumptions to limit the actual number of model parameters in the inversion and keep the inversion computationally tractable. In the end, the reduced set of dynamic model parameters to be determined by the inversion procedure are T_0 , a, b, f_0 , and L as 2D fields, and s_w and s_{ini} as 2D fields on the smaller (velocity-strengthening) portion of the fault. For the purposes of the inversion, we parametrize the spatial distribution on an equidistant grid of 12×9 control points, from which the parameters are bilinearly interpolated onto the grids for the dynamic and quasidynamic simulations. The 2D fields are supplemented by four more free parameters describing our nucleation procedure realized by a 1-s-long gradual increase of prestress in a circular zone—the position of its center, its radius, and the added stress.

2.1.4 Inverse problem

We formulate the inverse problem in the Bayesian framework [Gallovič et al., 2019a, Gallovič et al., 2020, Kostka et al., 2022]. We assume uniform prior PDFs for the model parameters in wide intervals of permissible values. The data are considered to have Gaussian distributions of errors with SDs of 5 cm and 2.5 mm for seismograms and GPS, respectively. We sample the posterior probabilities using the Markov chain Monte Carlo (MCMC) parallel tempering algorithm [Sambridge, 2013], accepting proposed models according to the Metropolis-Hastings rule. We used a modified version of the inversion code fd3d_tsn_pt. This code has been previously validated for slip-weakening friction law and only seismic

data using synthetic tests [Gallovič et al., 2019a] and applied to the 2016 Amatrice [Gallovič et al., 2019b] and 2020 Elazığ earthquakes [Gallovič et al., 2020]. The present application required implementing the modified forward model and parameters.

We model data from 10 near-source strong-motion accelerometers, seven continuous GPS stations, and four alignment arrays capturing surface fault offsets [Lienkaemper et al., 2016, McFarland et al., 2015] at vineyards crossing the fault (see Figure 3.1a for their position with respect to the fault). We consider the frequency range of 0.05 to 0.5 Hz for the seismograms and daily sampled GPS displacements (the original dataset from UNAVCO; `www.unavco.org`). Alignment array measurements were irregular in time, so we use all accessible data points from four sites where substantial afterslip was detected (initial measurements were 2 to 5 days after the earthquake, two more in the first 10 days, and two more between 10 and 30 days). Data from both GPS and alignment arrays are considered in the first 30 days after the earthquake.

We accelerated the inversion progress by starting from a reasonable model that was relatively homogeneous with velocity-weakening friction at the central square-shaped portion of the fault and velocity-strengthening friction on all edges. From there, we allowed the parallel tempering MCMC approach to explore the model space. We manually intervened several times by optimizing the prestress, nucleation, and frictional parameters to find a model with positive variance reduction. After that, we explored the model space by running the MCMC sampling on an IT4I cluster with four Nvidia Tesla V100 GPUs and in-house computers with three GPUs (Nvidia 2080Ti), with each forward simulation taking about 40 s in both cases. The total number of visited models was high ($\sim$500,000). The final set consists of $\sim$7500 accepted models with a posterior probability density value larger than 5% of the pPDF maximum.

We also use the method of Gallovič et al. [2019a] to perform the SW dynamic inversion. We maintain as many features of the presented FVW problem as possible, including the finite difference setup (discretization, domain size), fault geometry (size and orientation of the fault), velocity model, and the positions of both seismic and GPS stations. We exclude the postseismic data as SW friction cannot model the postseismic phase. We include zero coseismic displacements at the positions of the southern alignment fields NLAR and NWIT, where no coseismic rupture was observed.

Following Gallovič et al. [2019a], we parametrize the dynamic model by spatial distributions of three dynamic parameters: shear (horizontal) prestress T_0, breakdown friction drop $\Delta f = f_s - f_d$ and slip-weakening distance D_c, while the dynamic friction is set constant $f_d = 0.4$. See Figure 2.1 and the related commentary for more details about the SW friction law and its parameters. The dynamic parameters are sought on the fault in a coarse 12x9 grid of control points at the same positions as in the FVW inversion.

2.2 FD3D_TSN code

The FD operators in FD3D_TSN are adapted and extended from the 3D FD code FD3D by R. Madariaga [Madariaga et al., 1998]. They utilize regular cubic grids, and are relatively simple and computationally efficient [Levander, 1988]. Their

use leads to a high speed of the calculation and is allowed by considering a simple fault geometry. Discontinuous velocity components at the fault are antisymmetric, allowing for the simplification of the fault boundary condition. Consequently, only one side of the fault needs to be calculated, cutting the required computational capacities (central processing unit [CPU] time and memory storage) in half. The major factor influencing the accuracy of FD3D_TSN is the here used implementation of the fault boundary condition. We use the traction-at-split-node approach [Dalguer and Day, 2007], which leads to an accuracy comparable with other codes.

Although many rupture propagation codes provide parallelization using OpenMP and Message Passing Interface (MPI), graphic processing units (GPU) acceleration is gaining attention only recently. GPU acceleration of wave propagation codes using FD and finite-element methods was implemented by Michéa and Komatitsch [2010] and Komatitsch et al. [2009] using Compute Unified Device Architecture (CUDA). CUDA is also featured by the publicly available spectral element code SPECFEM3D [Komatitsch et al., 2010] and the FD code AWP-ODC [Zhou et al., 2013]. The RAJA library is used to accelerate the SW4 code [Rodgers et al., 2019].

To foster the GPU acceleration in the field of rupture dynamics, we utilize the easy-to-use OpenACC approach to optionally port the code to GPUs. We demonstrate that the speed-up can be significant, by one order of magnitude when using commonly available GPUs. We note that OpenACC, in comparison to the CUDA framework, allows also for non-Nvidia accelerator support, whichwill become increasingly important as demonstrated by future U.S. exascale machines relying on AMD GPU accelerators.

FD3D_TSN works with any horizontally layered 1D velocity model; its parameters are saved in the file crustal.dat. File inputfd3d.dat contains the information necessary for the initialization of the FD discretization and the PMLs, namely the size of the grid, discretization intervals in space and time, and PML thickness and damping. Because the source geometry is simple (2D planar and vertical), hard-coding another model, including its potential parameterization, is straightforward. This way, the code can be easily adapted for various user's needs such as a specific parametric study or a particular dynamic inversion.

2.3 Verification exercise and performance

We have performed several exercises from the community benchmark suite of the SCEC/USGS Spontaneous Rupture Code Verification Project [Harris et al., 2018]. Their main webpage (`http://scecdata.usc.edu/cvws/`) contains descriptions of the exercises and results generated by 5—20 different solvers, depending on the exercise. There are three types of results for comparison: time evolution of physical quantities at prescribed points on the fault (slip, slip rate, shear stress, and state variable if applicable), seismograms at off-fault positions, and rupture time contour plots, that is, lines showing the rupture tip position at every half second. Here, we present our results for benchmarks TPV5 (slip-weakening friction) and TPV104 (fast-velocity-weakening friction). In addition, the results for the TPV8 and TPV9 benchmarks can be found on the SCEC/USGS webpage.

For the TPV5 benchmark, the size of the computational domain is 31×10

× 15:5 km, whereas, for the TPV104 benchmark, it is larger (40 × 10 × 20 km) because the model contains additional velocity-strengthening layers around the fault following the benchmark definition. Figures 2.2 and 2.3 display results for TPV5 (spatial grid step $\Delta h = 100$ m) and TVP104 (spatial grid step $\Delta h = 50$ m), respectively. They are presented in terms of the rupture time contours along the fault and the on-fault slip rate and shear–stress time series at two locations.

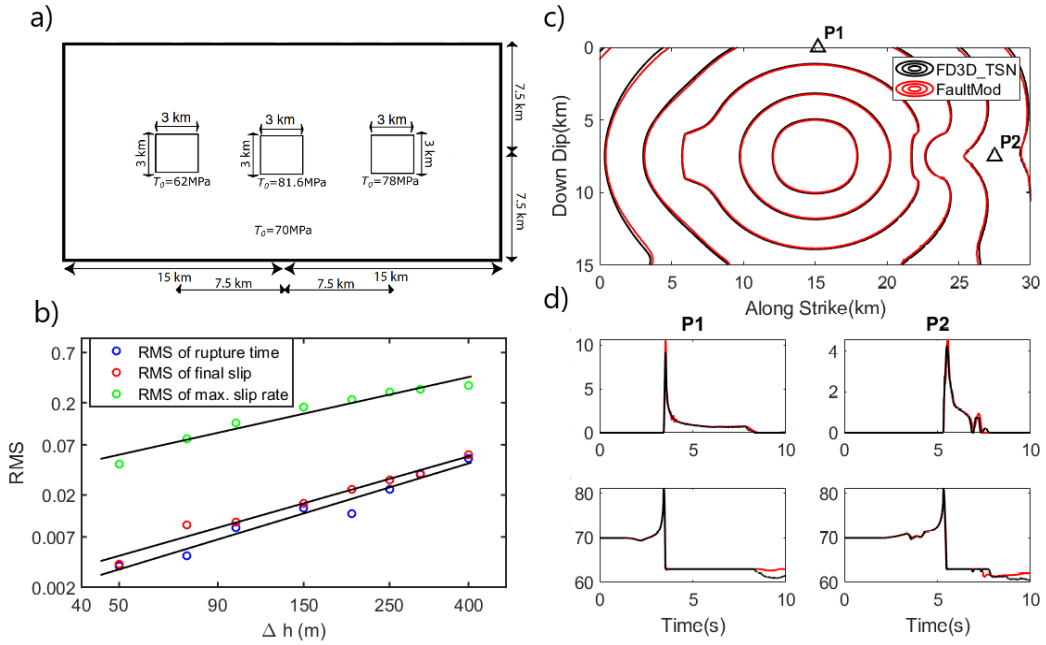

Figure 2.2: Results for the TPV5 benchmark (heterogenous prestress). (a) Schematic showing dimensions of the fault and positions of prestress heterogeneities T 0 (adopted from the Southern California Earthquake Center and U.S. Geological Survey [SCEC/USGS] benchmark webpage). (b) A plot of the root mean square (RMS) difference of the rupture time, slip, and maximum slip rate relative to a solution with $\Delta h = 25$ m as a function of Δh for FD3D_TSN. (c) Rupture front contours on the fault plane every 1 s. (d) Slip rates and shear stress (equal to the horizontal component of traction) at points P1 and P2, corresponding to fault receivers 'st000dp000' and 'st120dp075' in Harris et al. [2018]. For their position, see panel (a). Simulation results for FD3D_TSN with $\Delta h = 100$ m and SeisSol [Pelties et al., 2012] are denoted by black and red lines, respectively.

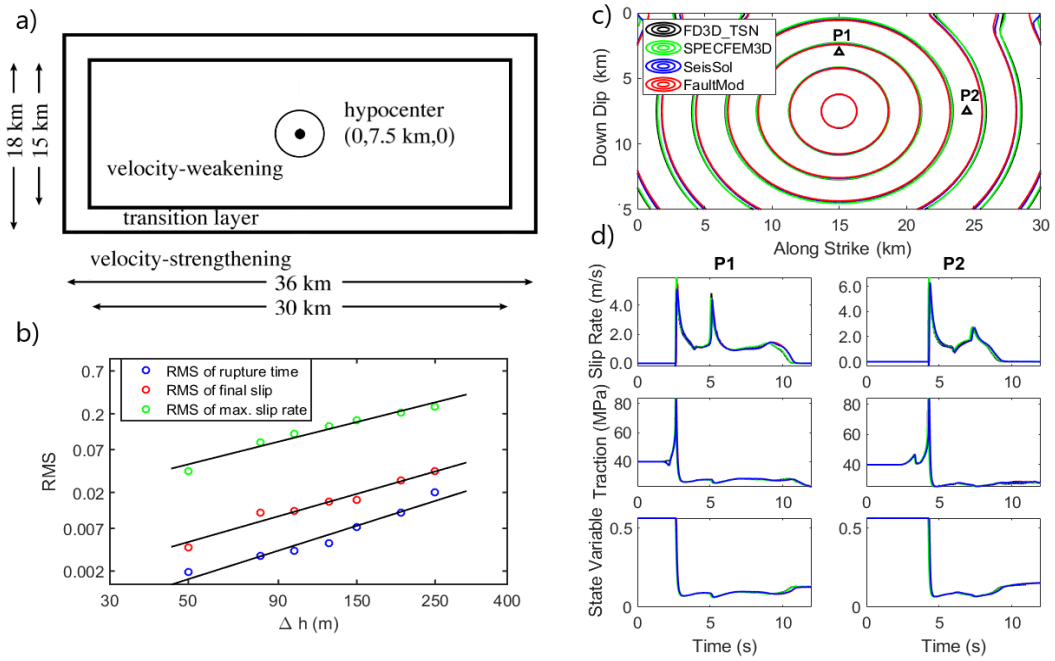

Figure 2.3: Same as Figure 2.2 but for the rate-and-state friction TPV104 benchmark. (a) Schematic diagram of the dimensions of the fault and positions of the velocity-weakening and strengthening zones (rectangles) and the nucleation zone (circle), as adopted from the SCEC/USGS webpage. (b) A plot of the root mean square (RMS) difference of the rupture time, slip, and maximum slip rate relative to a solution with $\Delta h = 25$ m as a function of Δh for FD3D_TSN. (c) Rupture front contours on the fault plane every 1 s. (d) The time evolution of the state variable. Solutions of FD3D_TSN with $\Delta h = 50$ m (black line), SPECFEM3d (green line), SeisSol (red line), and FaultMod (blue line) are shown. Nodes P1 and P2 correspond to fault receivers 'faultst000dp030' and 'faultst090dp075', respectively.

In both TPV5 and TVP104, the difference between the results of FD3D_TSN and code SeisSol [Heinecke et al., 2014, Pelties et al., 2014, Uphoff et al., 2017] are well within the typical variation among other solvers [Harris et al., 2009, 2011, 2018, Barall and Harris, 2015]. We note that the full set of the FD3D_TSN simulation results are uploaded in the benchmark database of solutions. At the benchmark website, our solutions can be compared with other code outputs and physical quantities on and off the fault.

We note small differences in rupture times for different solvers in the fast-velocity-weakening friction benchmark TPV104. The solution of FD3D_TSN agrees very well with that of SPECFEM3D [Kaneko et al., 2008], whereas the solutions of FaultMod [Barall, 2006] and SeisSol show slightly slower rupture (Figure 2.2). These differences remain visible with mesh refinement (compare to the $\Delta h = 50$ m solution). We understand these differences as an expression of differences in the implementation of rate-and-state friction evolution, but not restricted to staggered grid-specific choices.

Following Day et al. [2005], we calculate the root mean square (RMS) difference of the spatially averaged slip, rupture time, and peak slip rate for various grid sizes Δh relative to a high-resolution reference solution with $\Delta h = 25$ m,

Discrete Step (m)	**Degrees of Freedom × Timesteps (RAM Requirement)**	**Single-Core Wall Clock Time (s)**	**GPU-Accelerated Wall Clock Time (s)**
100	54,558,900 × 3000 (210 MB)	0:3:12	0:0:22
50	389,491,200 × 6000 (1490 MB)	0:39:13	0:3:47

Table 2.1: Wall clock times of the FD3D_TSN code for the TPV5 benchmark model, shown for two finite-difference (FD) spatial discretizations and for single core (Intel i9-9900K) and GPU-accelerated versions (Nvidia RTX 2700)

see b panels in Figures 2.2 and 2.3. Spatial discretizations $\Delta h = 100$ m and $\Delta h = 50$ m for benchmarks TPV5 and TPV104, respectively, are chosen for providing results sufficiently close to the reference solution (both rupture time and slip RMS measures are less than 1%). The slopes of the RMS misfits from both benchmarks are $-1/1$, $-1/2$, and $-1/3$ for maximum slip rate, slip, and rupture time, respectively.

Wall clock times of the code for both grid spacings Δh and TPV5 problem are shown in Table 2.1, both for the serial (running on one CPU core) and GPU-accelerated versions. We used CPU Intel i9-9900K and GPU Nvidia RTX 2070 hardware to run these tests. When using the GPU, it is essential to keep all variables in the GPU memory, because any data transfer to and from GPU memory is the major bottleneck affecting the overall speed of simulation. The amount of GPU memory is generally smaller (several GB) than the computer RAM, which limits the maximum size of the model. Memory requirements of these simulations were comfortably below this limit of 8 GB for Nvidia RTX 2070, see Table 2.1 for details.

3. Bridging time scales of faulting: from coseismic to postseismic slip of the 2014 South Napa earthquake

We provide a unifying dynamic model of the 2014 South Napa coseismic rupture and subsequent afterslip based on rate-and-state friction with fast-velocity-weakening effect [Dunham et al., 2011] included. The inferred rupture properties reconcile and refine previous independent studies. In addition, the dynamic inversion results enable previously unexplored physical interpretations of the connection between lithology and friction properties, and insights into the role of enhanced weakening in rupture propagation and on the mechanisms of coexistence of seismic and aseismic slip on a fault.

3.1 Results

Our Bayesian dynamic inversion aims at constraining the friction parameters and initial fault stresses that govern the space-time evolution of both seismic and postseismic slip and produce ground motions consistent with seismic and geodetic data. We assume a vertical planar fault of 20 km $\times$ 15 km size that reaches the surface and has a strike of 165° (Figure 3.1a), which is a simplified representation of the geometry constrained by the position of the surface rupture and relocated aftershocks [Hardebeck and Shelly, 2016]. The friction law, simulation techniques, data errors, model parameterization, and sampling of the posterior probability density function (pPDF) are described in preceeding Chapter. The result of the inversion is an ensemble of models with spatially varying dynamic rupture parameters, statistically representing samples of the pPDF.

Figure 3.1 (b and c) compares the coseismic data with our best-fitting model, which has a variance reduction of 0.49 for seismograms. The figure also displays the statistical variability of the simulated data due to the model uncertainty using kernel density estimates (KDEs) of the posteriors. The fit is generally good; we attribute the major portion of the data misfit to unmodeled 3D Earth structure in the velocity model and nonplanar nonvertical geometry of the real fault. Postseismic displacements at GPS stations and alignment arrays are displayed in Figure 3.1, d and e, respectively. We note that the displacements recorded by the GPS stations are of the order of 1 cm only due to the rather large distance of the stations from the fault and the moderate size of the earthquake. Nevertheless, the fit is still good despite postseismic displacement amplitudes being much lower than amplitudes of seismograms or alignment array displacements. The fit of the coseismic GPS displacements used for verification is comparable with the fit of those used for inversion. The surface slip measurements provide major constraints on afterslip. They are fitted very well due to their relatively high implicit weights in the inversion and lack of direct trade-offs with the other data. The total variance reduction of all GPS data is 0.63.

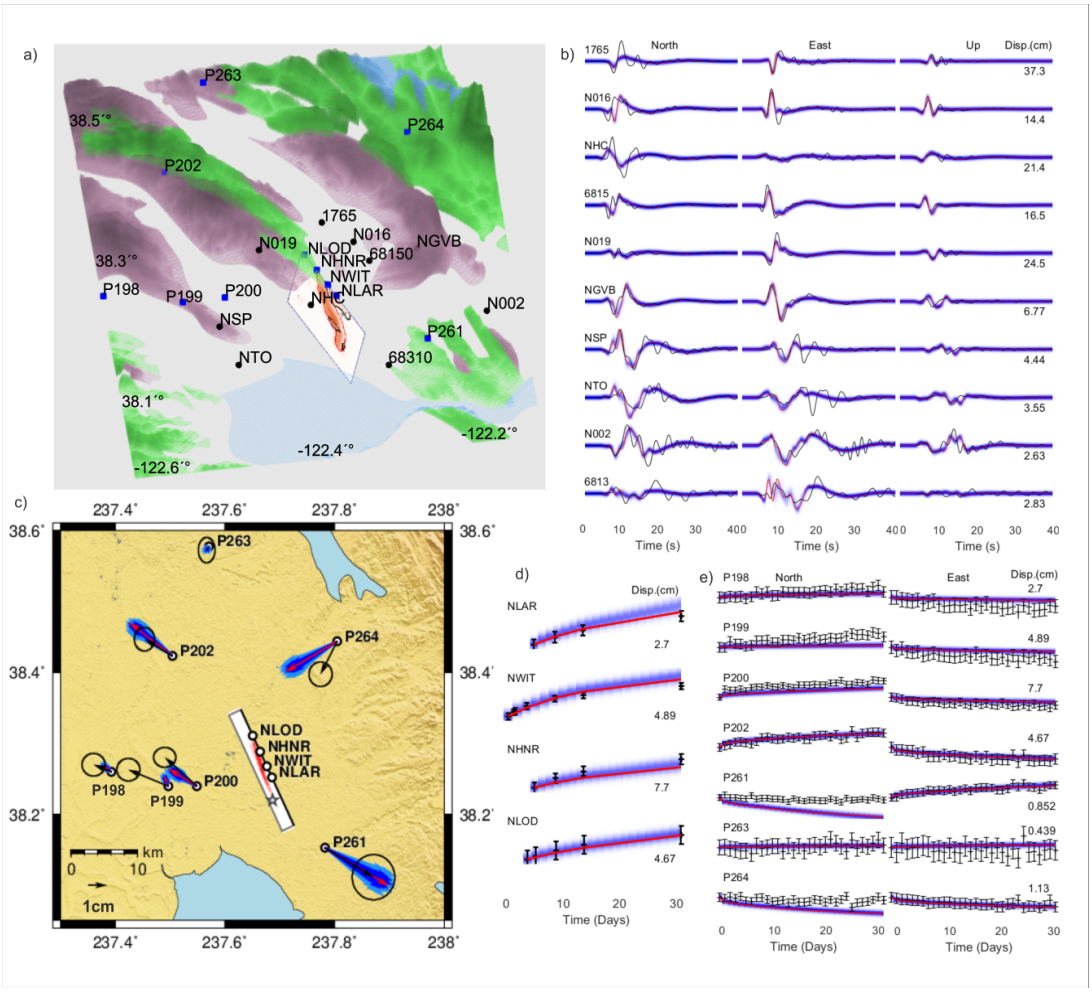

Figure 3.1: Maps and fits of coseismic and postseismic data. (a) Position of the fault with respect to the local geologic conditions (white, Quaternary sediments; green, Cretaceous rocks; purple, Cenozoic volcanic rocks), based on (27, 71) and seismic (black circles) and GPS (blue squares) stations. (b) Comparison between observed seismograms (black) and our best-fitting model seismograms (red). Kernel density estimates (KDEs) of the posteriors are displayed in blue. Station names and maximum displacements are indicated on the left and right, respectively. (c) Fit between observed coseismic GPS displacements (black arrows) and synthetic data (red arrows); KDEs are displayed in blue. Positions of the stations with their names are shown on the map (black circles) with respect to the fault (white rectangle), with total slip color-coded in white to red. Star denotes the epicenter. (d) Comparison between observed postseismic surface displacement (black) and our best-fitting model GPS (red). KDEs are displayed in blue, while errors of real data are shown as error bars. Station names are indicated on the left, and maximum displacements in centimeters are indicated on the right. (e) Comparison between observed postseismic GPS displacements (black) and our best-fitting model synthetics (red). KDEs are displayed in blue, while errors of real data are shown as error bars. Station names and maximum displacements are indicated on the left and right, respectively.

3.1.1 Kinematic and frictional properties and stress drop

Coseismic ruptures in our model ensemble nucleate at a mean depth of 10.46 ± 0.30 km and propagate upward and to the north. They create two major patches of coseismic slip at 3 and 6 km depths (Figure 3.2a), coinciding with the maximum stress drop areas, which locally reach 50 MPa (Figure 3.2d). The coseismic rupture propagates for about 8 s at an average speed of ∼2.4 km/s, releasing a seismic moment of (1.97 ± 0.10) × 10^{18} Nm. More than 90% (1.9 × 10^{18} Nm) of the moment is released within the first 5 s. Rise time fluctuates between 0.5 and 1 s and increases above 1 s in the shallowest 2 km. The rupture reaches the surface, over a length of more than 5 km. The final ruptured area attains a ribbon-like shape of width ∼5 km and length ∼12 km, and its major axis shows an unusual oblique orientation. Areas of shear stress increase (Figure 3.2d) concentrate around the rupture edges.

Postseismic slip evolves continuously after the coseismic slip around most of the rupture area. In particular, shallow afterslip starts within 20 to 24 hours from the southern side of the coseismic rupture (∼8 km along strike; see Figure 3.2b) and expands rapidly in the first 3 days at ∼1.5 km/day toward the south. Expansion continues over the whole modeled period of 30 days, albeit with decreasing rate. This produces a substantial (∼14 MPa) postseismic stress drop comparable with coseismic stress drop at the same depths. We also observe ∼10 cm of shallow postseismic slip even at the northern (coseismically ruptured) portion of the fault (Figure 3.2, a and b), in agreement with the shallow slip measurements [Lienkaemper et al., 2016]. Smaller patches of notable afterslip (with a maximum of ∼0.4 m) are located at about 7.5 km depth, partially overlapping with coseismic rupture. Some of our models show additional patches of afterslip further away from the earthquake, which we consider unconstrained due to their highly variable occurrence among models and minimal impact on synthetic data. Overall, the postseismic slip increases the total seismic moment of the earthquake by ∼40%, with a ∼15% increase happening during the first day after the earthquake.

The rupture properties described above stem from the dynamic rupture models, whose parameters are constrained by the inversion. A parameter of particular interest is $(b-a)$, which quantifies the relative importance between direct and evolution effects of rate-and-state friction, and controls the stability of slip: Positive values are associated with velocity-weakening frictional behavior and unstable slip, while negative values imply velocity strengthening and stable slip. Another important dynamic parameter is initial shear stress T_0. We show ensemble averages of spatial distributions of $(b-a)$ and $T0$ along the fault in Figure 3.3 (a and b) and their uncertainties in Figure 3.3 (c and d), respectively. We discuss only dynamic parameters in the slip area and closely adjoining regions of the fault, where we can consider them well constrained by data, we also show depth profiles of selected parameters in Figure 3.3e, calculated as horizontal averages over the slip region.

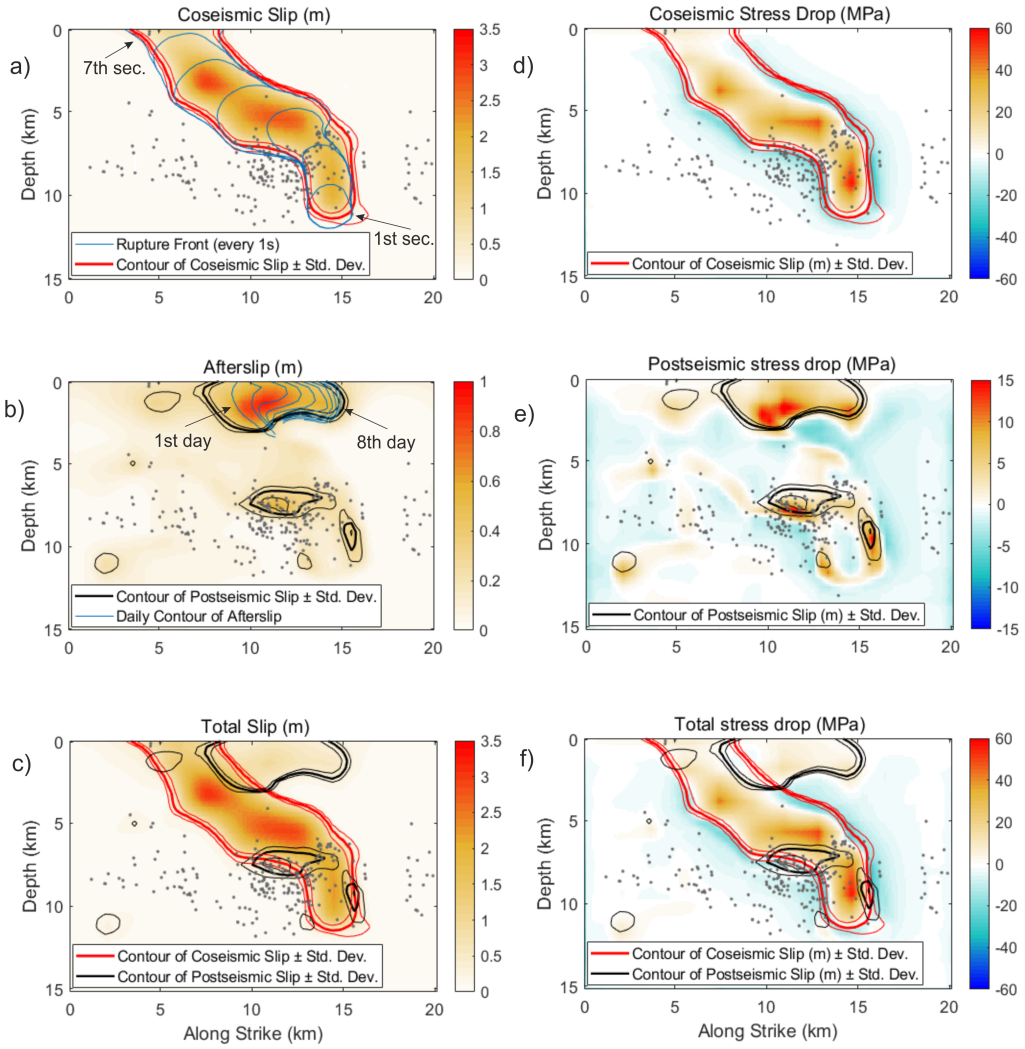

Figure 3.2: Kinematic rupture parameters and their statistics. Ensemble averages of (a) coseismic slip, (b) afterslip, and (c) total slip on the fault. Blue lines in the coseismic slip and afterslip map indicate the rupture front and the tip of the shallow afterslip in 1-day increments after the coseismic rupture, respectively. Ensemble averages of (d) coseismic, (e) postseismic, and (f) total stress drop. Contours (threshold of 0.3 m) of slip (red) and afterslip (black) with thinner lines denoting SD are displayed in all six panels. Gray dots represent aftershocks (Northern California Earthquake Data Center) with a fault-perpendicular distance of <5 km.

Stresses in the shallow zone, above 5 km depth, decrease with decreasing depth. The shallow zone hosts a combination of frictional parameters that limit rupture propagation and stabilize the fault, reducing both rupture speed and peak slip rates: velocity-strengthening rheology, increasing characteristic slip distance L up to ∼1.5 m, weakening velocity up to 3 m/s, and values of reference friction f_0 above 1. We note that the large values of f_0 found at shallow depth are unusual for rocks but can be attributed to cohesion. The horizontal transition zone between coseismic and postseismic rupture areas (7 to 12 km along strike)

is characterized by low prestress and more velocity-neutral friction ($b - a$ close to zero), and overlaps with both a change in lithology and a geometrical feature where the mapped fault starts to bend more toward the west. The strengthening rheology of the afterslip area is more pronounced in the south with $(b-a)$ ∼-0.01 as opposed to -0.005 in the northern part. At greater depths (Figure 3.3e), the main coseismic rupture area is dominated by velocity-weakening friction ($b - a > 0$), low values of the rate-and-state characteristic slip distance L ∼0.25 m, and weakening velocity 0.1 m/s, while reference friction f_0 is still relatively high (∼0.75).

Substantial heterogeneity in dynamic parameters exists around the 7.5 km depth overlapping with the patch of notable deep afterslip. Friction becomes velocity strengthening due to the increase in a, while f_0 decreases to 0.55. Other dynamic parameters (L,weakening velocity) have values similar to those in the coseismic region. The fracture and radiated energies are (9.2 ± 0.8) and (4.5 ± 0.7) MJ/m 2, respectively. The radiation efficiency of the earthquake is thus 0.33 ± 0.11.

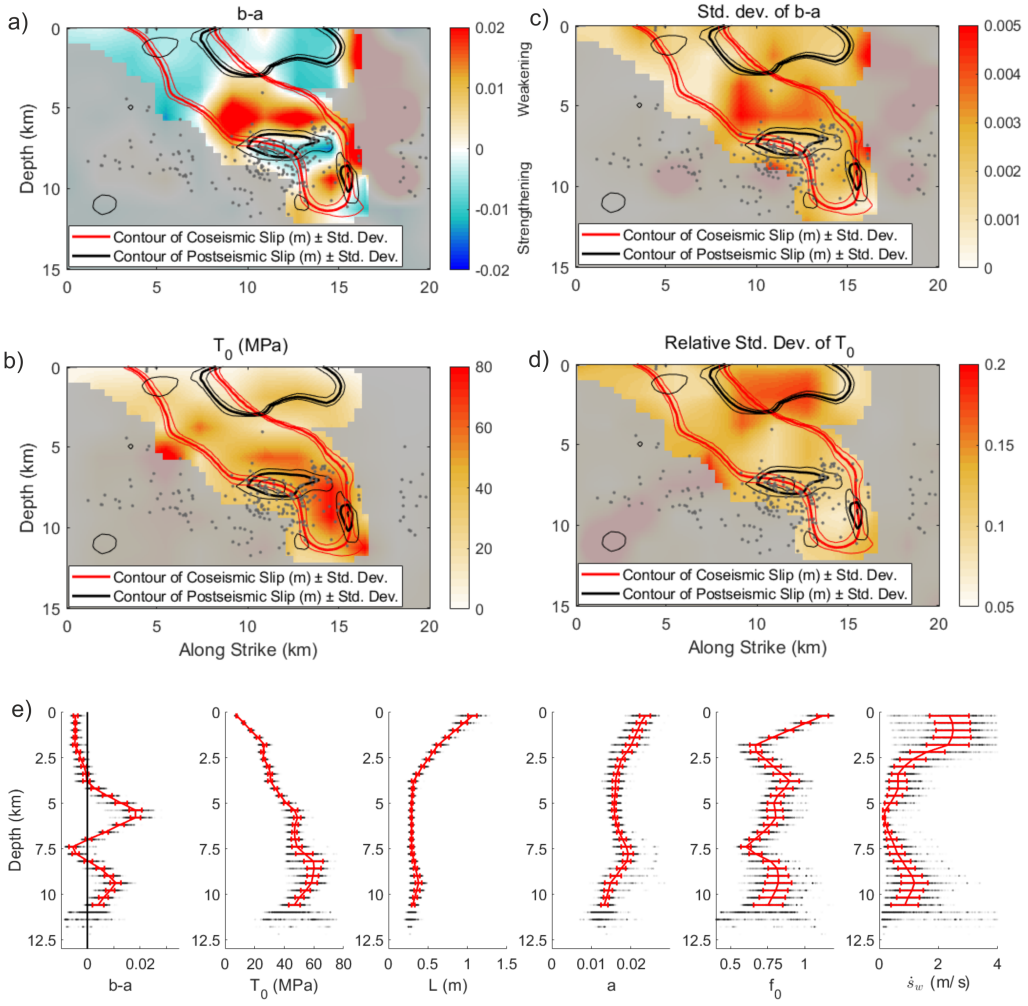

Figure 3.3: Selected dynamic parameters and their statistical properties. (a) Ensemble average of $(b-a)$. Gray dots denote the aftershocks as in Figure 3.2. Red and black lines indicate contours of slip and afterslip, respectively. (b) SD of $(b-a)$. (c) Same as (a) but for prestress T_0 . (d) Same as (b) but for relative SD of T_0. (e) Horizontal averages of $(b-a)$, T_0, characteristic slip L, a, reference friction f_0, and weakening velocity $\dot{s}_0$ on the ruptured part of the fault. Black dots denote averages of individual ensemble models, while the red line with error bars show ensemble mean and SD, respectively. Vertical black line denotes $(b-a) = 0$.

3.2 Discussion

We have conducted a Bayesian dynamic inversion of the 2014 South Napa earthquake, creating a set of ∼7500 models that help explain both coseismic and postseismic data in a unified framework of the rate-and-state fast-velocity-weakening friction law. The model describes frictional behavior over a wide range of time scales, from coseismic seconds to postseismic weeks. The simulations are enabled by a combination of fully dynamic and quasidynamic modeling of the coseismic

and postseismic phases, respectively. The resulting main source features are consistent with those identified by previous analyses of the coseismic and postseismic data. In particular, the inferred coseismic upward and northward rupture propagation with two main patches of slip and the position of substantial shallow afterslip are consistent with published measurements [Lienkaemper et al., 2016, DeLong et al., 2016, Brooks et al., 2017] and kinematic models [Floyd et al., 2016, Dreger et al., 2015, Ji et al., 2015, Wei et al., 2015, Barnhart et al., 2015].

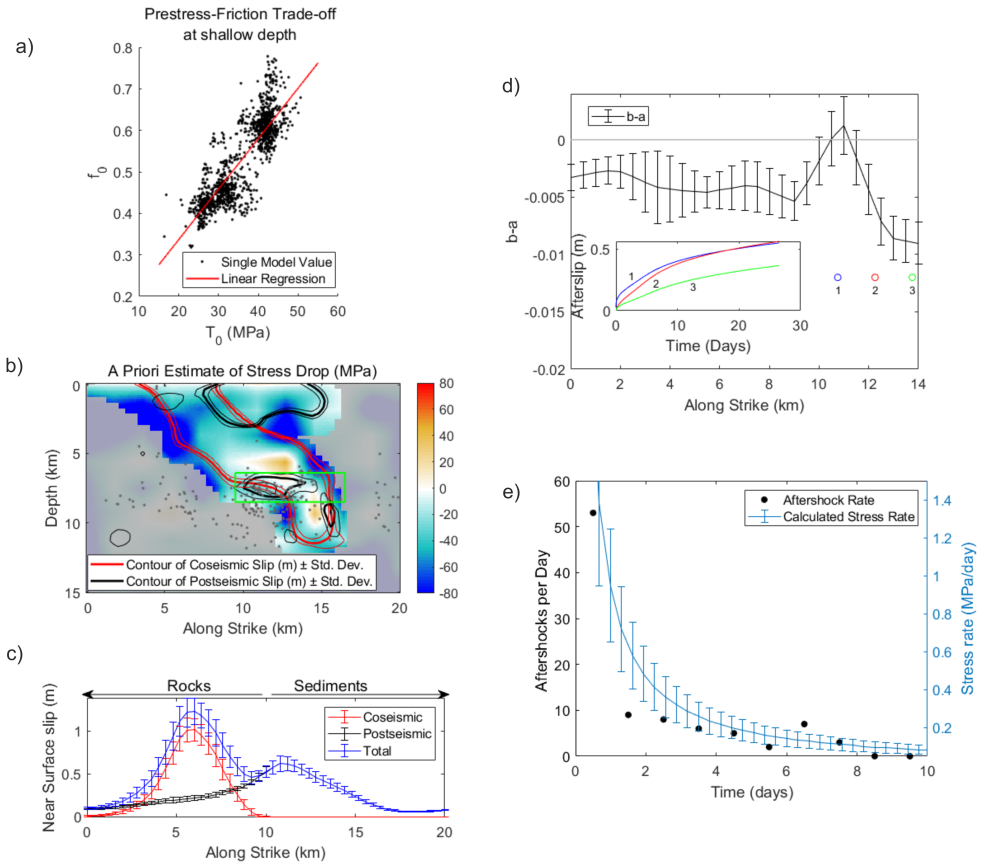

Figure 3.4: Plots documenting various modeling features for discussion. (a) Scatter plot of local dependence between T_0 and f_0 at a position located 11.5 km along strike and at 1.5 km depth. (b) A priori estimate of dynamic stress drop calculated as prestress T_0 minus steady-state friction with f_{SS} at $\dot{s} = 0.1$ m/s as friction coefficient. (c) Along strike distribution of coseismic slip (red), afterslip (black), and total slip (blue) at 200 m depth. Error bars denote the ensemble mean and SD. (d) Ensemble mean and SD of $(b - a)$ at 200 m depth. Circles denote the along-strike position of three points, for which the inset shows the afterslip development. (e) Development of stress rate (error bars showing ensemble mean and SD) and the number of aftershocks per day (black points) in the deep postseismically slipping area denoted by the green rectangle in (b).

The joint modeling of earthquake slip and afterslip allows us to constrain dynamic parameters on larger portions of the fault than only coseismic dynamic inversion would. This is enabled by the fact that inferred coseismic and postseismic slip are spatially complementary, although some afterslip takes place in the

coseismic area, especially near its border. The central part of the coseismic zone is dominated by velocity-weakening ($b - a > 0$) friction. Still, the rupture also propagates through velocity-strengthening ($b - a < 0$) areas near the free surface and above the hypocenter at about 7.5 km depth. The shallow zone is of particular interest because it hosts a transition from seismic to aseismic slip, which occurs over a short distance of 1 km, in agreement with the surface measurements. In addition, the shallow afterslip rate is spatially heterogeneous, being faster near the coseismic zone than further away. These complexities are encoded in the dynamic parameters, in particular $(b - a)$. The deeper strengthening zone not only ruptured coseismically but also hosted notable afterslip, triggering aftershocks off the fault and below the coseismic rupture. Below we discuss and interpret those important features in detail.

3.2.1 Interplay between coseismic and postseismic ruptures at shallow depths

The unique feature of our modeling is to adopt a single friction law for both the coseismic and postseismic ruptures, in contrast to their independent treatment in previous works [e.g., Langbein et al., 2006, Fukuda et al., 2009, Twardzik et al., 2021]. In the case of the South Napa earthquake, the shallow zone above 3 km depth hosts an abrupt horizontal change from seismic to aseismic rupture. The northern portion of the shallow fault ruptured coseismically, switching within ∼1 km to the south to primarily postseismic rupture (Figure 3.3b). The total shallow slip (coseismic and postseismic) has two local maxima, one in the coseismic zone at around 6 km along strike and one in the postseismic zone at 11 km along strike (Figure 3.4c). The local minimum (∼9 km along strike) coincides with the border between the coseismic and postseismic slip areas and is associated also with nearly zero total stress drop (Figure 3.2f). These characteristics are well constrained by data from the alignment arrays and are in good agreement with previous models of shallow slip [e.g., Lienkaemper et al., 2016].

The distribution of frictional properties in our results (Figures 3.3b and 3.4b) shows that the whole shallow part of the fault is velocity strengthening, including the coseismic portion. This feature of rate-and-state dynamic models is implied by physical mechanisms (low normal stresses, temperature, and unconsolidated gouge) described in Introduction. Further modeling investigations [Kaneko et al., 2008] suggest that this shallow layer substantially reduces the potential for large coseismic surface rupture and accompanying large seismic wave radiation (unusual for natural earthquakes) in comparison with purely velocity-weakening models.

The along-strike distribution of $(b - a)$ (Figures 3.4d) shows a clear difference between the coseismic (∼-0.005) and postseismic (∼-0.01) areas. This change in $(b - a)$ coincides with the transition between Cretaceous rocks to the north and younger Quaternary sediments in the south (Figures 3.1a and 3.4a). As the unusual properties of the 2014 South Napa earthquake (shallow afterslip, position of the coseismic slip) are at least partially governed by this change in frictional rheology, the rupture propagation was clearly affected by the transition between the two lithological units. This division between Cretaceous rocks and Quaternary sediments happens only in the near surface region, while the rest of coseismic slip occurred at larger depths where the lithology is composed of Cretaceous rocks

[Graymer et al., 2006]. After the coseismic rupture propagates through this deeper area and arrives at the shallow layer, it continues only in the rock (northern) part of the fault, being impeded in the (southern) sedimentary part of the fault where a complementary afterslip develops subsequently. We suggest this mechanism to be responsible for the ribbon-like shape of the coseismic rupture.

3.2.2 Variability in the shallow postseismic slip

The evolution of shallow postseismic slip is spatially heterogeneous. Figure 3.4d shows the afterslip at three nearby points located from 10 to 15 km along strike. The temporal behavior varies in both amplitude and characteristic decay time. This is well constrained by the surface data and was also identified in kinematic inversions of afterslip [Floyd et al., 2016]. In our dynamic model, the difference is facilitated by along-strike variations of $(b-a)$ (see Figure 3.4d). The value of $(b-a)$ affects the time scales over which afterslip develops, as can be seen from a simple spring slider model [Marone et al., 1991, Perfettini and Avouac, 2004, Perfettini and Ampuero, 2008], for which afterslip $s(t)$ develops logarithmically with time t

$$s(t) = \sigma_n \frac{a-b}{k} log(\frac{v_i t}{\sigma_n \frac{a-b}{k}} + 1) \tag{3.1}$$

In addition to $(b-a)$, the temporal evolution of afterslip depends on effective normal stress σ_n, stiffness k (that scales with shear modulus μ and the inverse of patch size), and initial velocity v_i. The normal stress and stiffness can be assumed constant in the horizontal direction (with the potential exception of lateral variations in fluid pressure that are beyond the scope of this paper), while the initial velocity is higher at the northern part, where the slip initiated during the coseismic phase.

We show the development of shallow afterslip in Figure 3.4d, as calculated at three points near the surface (at 200 m depth) located from 10 to 15 km along strike. The positions were chosen to show the impact of different values of $(b-a)$ changing from $\sim$0 to -0.01 over 2 km. Afterslip starts much quicker close to the coseismic rupture where $(b-a)$ is close to zero. The characteristic decay time of afterslip then clearly increases further to the south as $(b-a)$ approaches -0.01. The afterslip develops under non–steady-state conditions in 3D models, and therefore does not entirely conform to the simplified logarithmic formula derived for a 1D spring slider, but its basic properties do hold. This short-distance variability in afterslip is a further example of the strong impact of fault lithology on rupture development. Whether it is driven by small-scale changes in mineral composition or pore pressure along the boundary between rocks and sediments remains an open issue.

4. Comparative analysis of results from dynamic source inversions with different friction laws

The SW friction is a standard in the dynamic modeling community due to its relative simplicity (low amount of parameters, linear dependence of friction on slip). We are thus interested in how the dynamic inversion employing the SW friction compares with the FVW one. To that end, F. Gallovič performed a dynamic inversion of the same 2014 South Napa earthquake employing the SW friction with as similar set-up as possible. This puts us in a unique position to compare dynamic models employing either SW or FVW friction law to model data from the same earthquake. In this chapter, we aim to present and compare the results of both SW and FVW dynamic inversions.

The Bayesian dynamic inversion started from an independently prepared initial model and with wide homogeneous prior distributions of dynamic parameters. We note that slip-strengthening friction is not permitted with this choice of intervals. The Monte Carlo sampling method visited a large set of hundreds of thousends trial models, out of which $\sim$ 60000 were accepted by the Metropolis-Hastings algorithm, where the probability of acceptance of the model was proportional to the misfit between synthetic and real data (both seismograms and coseismic GPS). For this comparative analysis, we picked only models with seismogram variance reduction (VR) > 0.43, which further restricted the model ensemble to $\sim$45000 models. All models in the restricted ensemble model fit the seismograms similarly, with VR = 0.43-0.47. The seismogram fit reached by the models with SW friction is very similar to the results of the inversion using the FVW friction presented in Chapter 3.

4.1 Comparison of SW an FVW model ensembles

We show histograms of the gross physical parameters of both the SW and FVW model ensembles in Figure 4.1. The distribution of VR suggests that a lot of SW models has the seismogram VR closer to the lower boundary of VR = 0.43, in contrast with the FVW ensemble whose VR shows a bimodal distribution with maxima around 0.45 and 0.47. This difference between both ensembles might be a result of how the posterior sampling procedure performed with the different friction laws, because the FVW inversion has larger amount of free parameters and dataset enriched by postseismic data in comparison with the SW inversion.

Distributions in Figure 4.1 are usually unimodal, but in the SW case the stress drop, centroid depth and fracture energy show a bimodal distribution. Gross physical parameters from the FVW model ensemble are consistently larger than the SW ones, with the exception of the rupture area, which achieves very similar

value for both ensembles. Relative uncertainties are larger in the case of the SW ensemble with no exceptions. The spatial distributions of both kinematic and dynamic parameters from the SW and FVW inversions share many similarities. Namely we see a very similar spatial structure of both slip and stress drop with two distinct patches at 6 km and 3.5 km depths and small surface rupture in the southern (left) portion of the fault. This suggests the available data resolve this basic picture independently of the chosen friction law.

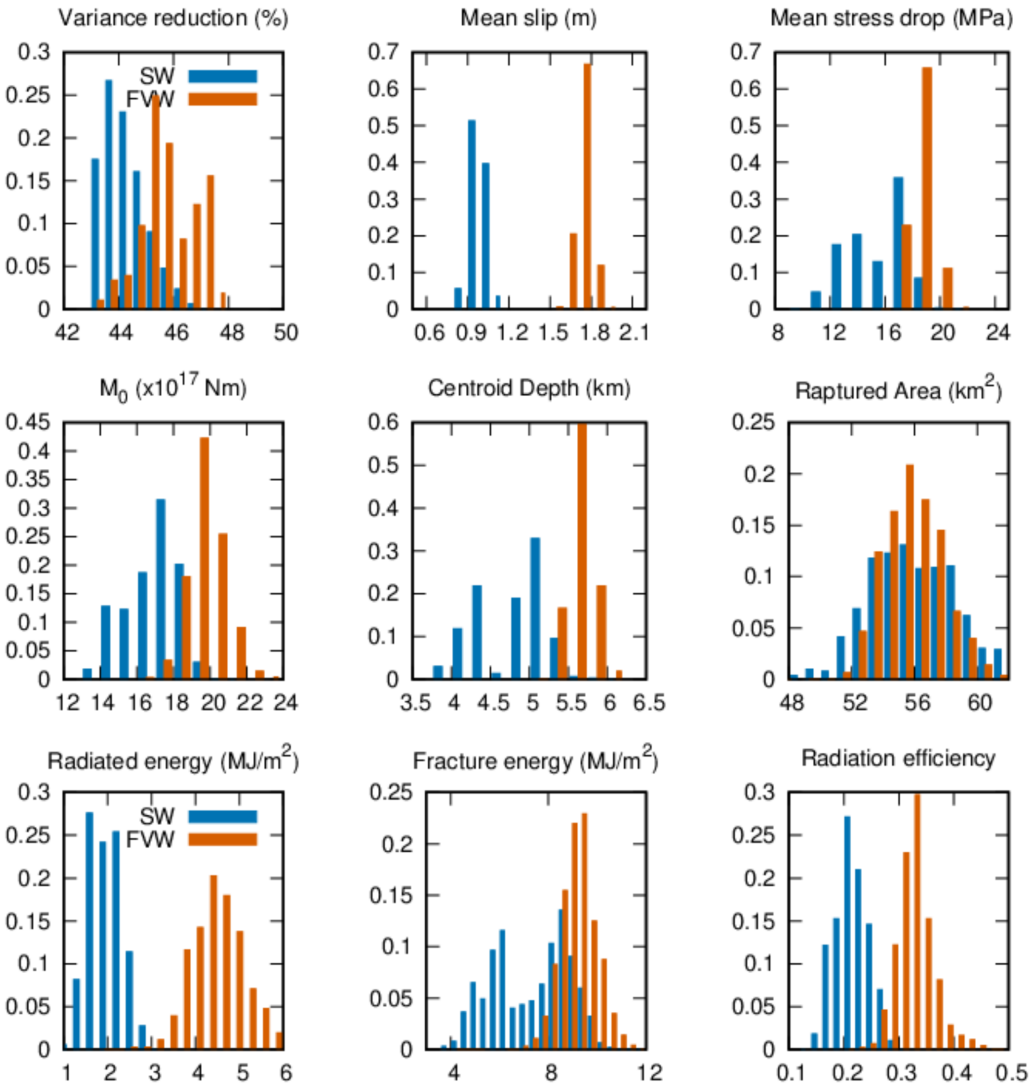

Figure 4.1: Histograms of gross physical parameters, see text for their definitions. Distributions from the SW and FVW inversion are shown as blue and red bars, respectively.

To study the differences between both ensembles in more detail, we compare the contours of coseismic slip from the SW ensemble with both coseismic and postseismic slip from the FVW ensemble in Figure 4.2. While the slip contours mostly overlap, there are discrepancies in the vertical positioning of the slip. The SW models occupy shallower depths than the FVW ones, especially in the southern half of the fault. This also manifests as the difference between the SW

and FVW average centroid depth h_c, where the SW model's centroid is positioned 900 m closer to the surface and with larger uncertainty than the FVW centroid.

SW slip is less constrained, which is clearly visible when comparing the distance between the SD contour lines and the line denoting the average slip in Figure 4.2, and the relatively large SD of centroid depth. As the size of the ruptured area is well constrained in both friction models, the higher uncertainty of the shallower border of the SW rupture leads to a similar uncertainty of the deeper border.

We suppose that the difference in the position of the coseismic slip is due to the absence of afterslip modeling in the SW inversion. As seismic and aseismic slip are mostly spatially separated [Marone et al., 1991], the area of shallow afterslip effectively blocks the spread of significant coseismic slip in the FVW inversion, see Figure 4.2. The only comparable constraint on the SW inversion is the zero coseismic slip in the NLAR and NWIT alignment fields, which only prevents very shallow slip at their positions.

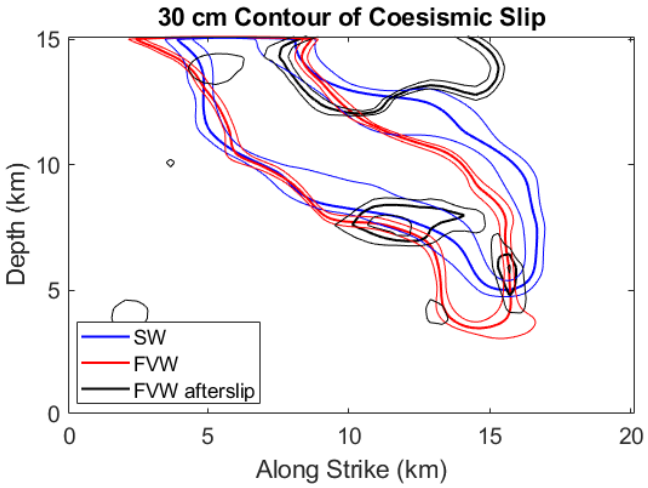

Figure 4.2: Contours of 30 cm slip of the coseismic SW and FVW slip and the FVW afterslip, see legend. Thick lines delineate ensemble averages and thin lines represent their SD.

Next, we investigate the impact of the depth of the slip (quantified as the centroid depth) on seismic moment and stress drop. We plot the values of stress drop and seismic moment from both ensembles as a scatter plot against centroid depth in Figure 4.3. It demonstrates a clear trade-off between the centroid depth and both seismic moment and stress drop, which are both higher for deeper models. While the trade-off occurs in both inversions, it is more pronounced in the SW one, see the slope of the linear regression lines in Figure 4.3. The SW seismic moment and stress drop ranges from 1.4 $\times 10^{18}$ to 2.1 $\times 10^{18}$ Nm and from 10 to 20 MPa, respectively. The intervals in the FVW ensemble are smaller, with the seismic moment from 1.7 $\times 10^{18}$ and 2.25 $\times 10^{18}$ Nm and stress drop from 17 to 21 MPa.

The fact that the SW models are less spatially constrained poses a challenge to further detailed comparison. It manifests as high uncertainty of both gross parameters and the spatial distributions of kinematic and dynamic parameters. The SW models with shallow centroid depth have coseismic slip at portions of the

fault that ruptured aseismically in the FVW inversion. As we already presented ample evidence for the occurrence of near-surface aseismic slip in Chapter 3, we consider the SW models coseismically rupturing the shallow aseismic part to contradict the observations. We notice in Figure 4.3, that there is a large amount of SW models with the centroid depth of around 5.5 km, overlaying with FVW models even in terms of the seismic moment (though still with slightly different stress drop). In the Thesis we further focus on this group of deeper-positioned SW models.

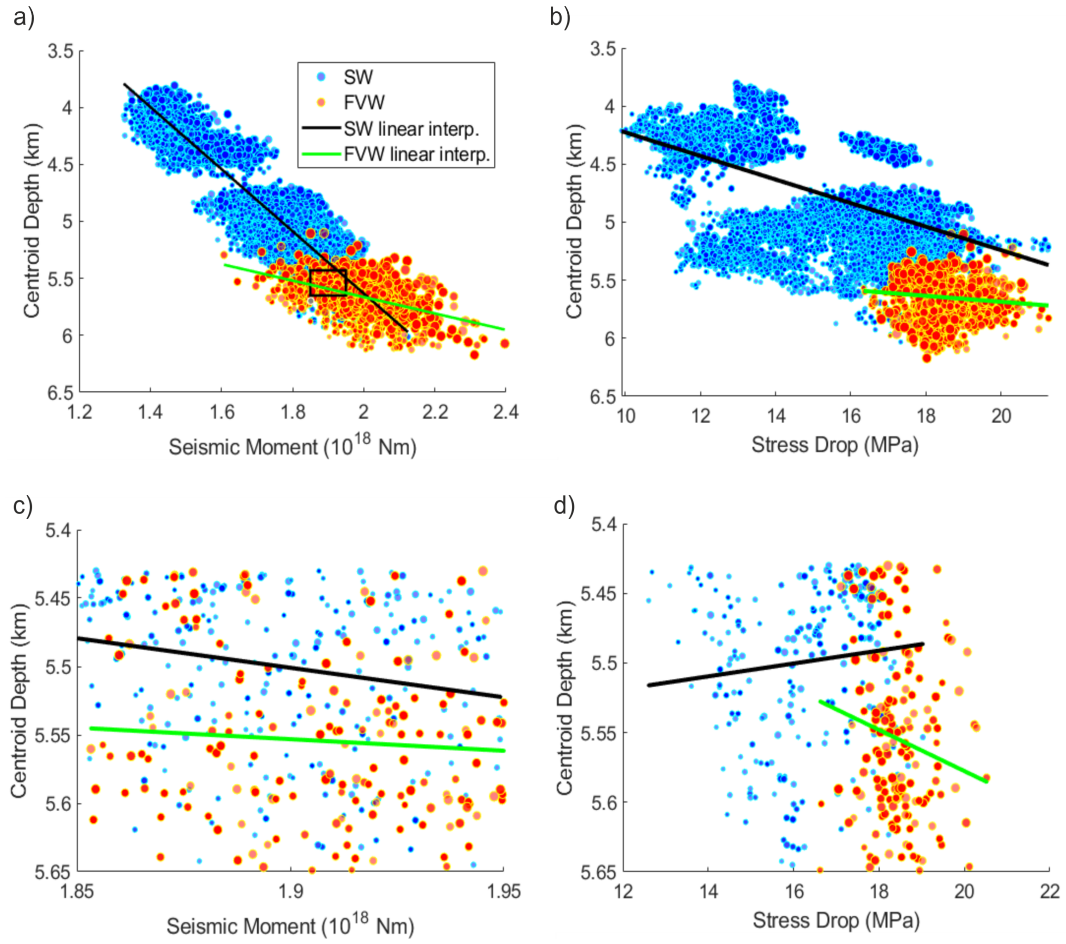

Figure 4.3: Ensemble scatter plot of (a) coseismic moment and (b) stress drop versus centroid depth. SW and FVW models are denoted by blue and red dots, respectively, with diameter proportional to the model variance reduction. The black rectangle in (a) denotes a selection of models, whose scatter plots are shown in panels (c) and (d), respectively. Lines shown linear regressions of the respective ensembles, see legend in panel a.

The physical mechanism behind the trade-offs of the seismic moment and stress drop with depth is the attenuation of seismic waves due to geometric spreading. To fit the seismogram amplitude with similar accuracy, the deeper earthquake needs to be larger in terms of seismic moment and stress drop. This mechanism is significant in the case of local stations used in the inversion as the difference in depth between earthquakes significantly changes the wave travel-distance (often more then 10%). The FVW model ensemble centroid depth is much better constrained, leading to a weaker trade-off between seismic moment

and h_c and overall lower SDs. This result underscores the importance of afterslip modeling as it may improve the resolution of coseismic slip.

5. Conclusions

This Thesis contributes to the development of inverse physics-based modeling of the earthquake source. Our study of the 2014 Napa earthquake in Chapter 3 reconciles and refines previous disjunct kinematic analyses of its coseismic and postseismic slip. We show how the stressing and frictional conditions on the fault govern the spatial separation between the shallow co- and postseismic slip. We determine that the earthquake created a rather narrow oblique rupture with postseismic slip spreading southwards, especially in the shallow area. This faulting complexity is driven by frictional rheology, supporting the hypothesis about the significant impact of heterogeneous lithology on rupture propagation [Floyd et al., 2016]. A particular, otherwise unrevealable feature, is that the coseismic rupture partially propagated through deep and shallow areas with velocity-strengthening frictional rheology (usually not supporting earthquake propagation), where postseismic afterslip occurred subsequently. We demonstrate that the deep afterslip was accompanied by off-fault aftershocks. We point out that since the co- and postseismic slip are only partially overlapping on the fault, the joint modeling allows us to constrain dynamic parameters on a larger portion of the fault than with coseismic data only.

Comparisons of the dynamic inversions with fast-velocity-weakening and slip-weakening friction laws in Chapter 4 lead to interesting conclusions. We see many similarities between the models, especially in the spatial distribution of slip and stress drop, or pulse-like evolution of the slip rate. In this sense, the results of the dynamic inversion seem to be better constrained than various kinematic inversions. Finding common properties of dynamic models across various friction laws is encouraging as the true friction law governing the tectonic faults remains elusive. We note that the elastodynamic equation is the common factor between both dynamic inversions, and can play a key role in constraining the source properties. The obvious advantage of the rate-and-state framework is the ability to model the aseismic slip unfolding after the earthquake. We show that this capability might be relevant even when estimating coseismic quantities (such as the distribution of slip, or the value of seismic moment), due to the tendency of seismic and aseismic slip to occur on the fault with limited overlap. The location of the aseismic slip can thus act as an additional constraint on the coseismic slip and other physical parameters of the earthquake.

The mathematical complexity and nonlinearity of the dynamic inversion make it a technically demanding task, which we identify as a critical reason why it is presently understudied. The requirements are not only in high computational demands but also in both the quantity and quality of data used in the inversion. The physics-based inverse modeling presented in this Thesis is enabled by the current technology both on the modeling and data-collection ends. We took advantage of modern hardware and developed highly-efficient GPU-optimized code FD3D_TSN [Premus et al., 2020]. Both FD3D_TSN and the whole Bayesian inversion package fd3d_pt_tsn are freely available at `https://github.com/JanPremus/fd3d_TSN` and `https://github.com/fgallovic/fd3d_tsn_pt`, respectively. Speed-up of the computation time of the forward modeling by a factor of 10 decreased the total time of our inversion from years to a more manageable 2-3 months on

common hardware. Additionally, the wealth of scientific recordings of the 2014 Napa earthquake is unique and almost unprecedented elsewhere in the world. We especially underscore the importance of the postseismic surface displacement measurements that acted as the major constraint on the shallow afterslip. The only earthquake of similar size with an equal or even better data set is the 2004 Parkfield earthquake also in California.

Limitations of our current approach mostly stem from the trade-off between the model complexity and its computational demands. The current version of the code can model only vertical and planar faults because it allowed us to use a very efficient finite difference method. Further expansion of the code towards modeling of, e.g., dipping faults would significantly expand the group of events we could study. Finite difference methods with curvilinear grids are a typical way of introducing non-planar faults, but they come with a high computational burden. To our knowledge, only Cruz-Atienza et al. [2007] introduced a stable non-planar fault into the regular, partially staggered grid code. An intriguing alternative to achieve the desired geometry of the problem is to dip the free surface instead of the fault, using a vacuum formulation for the free surface, e.g., from Graves [1996]. This idea was recently tested by Pitarka [2020] with promising results. We note, that the introduction of the dipping fault through this method would increase the computational burden of the forward model by a factor of 2-3 because it would be required to simulate the whole domain instead of the current half and the domain would have to be larger to encompass the whole fault and free surface.

The computational burden when introducing other model complexities would be even higher, which currently impedes the progress of physics-based inversions. A possible remedy might be improving the inversion method to decrease the number of visited forward models. Concerning the Bayesian formulation, we see an untapped potential in the prior distributions of dynamic parameters that are currently set in all control points as the same wide homogenous distributions. Potential improvements to these prior distributions include carefully assimilating information from preceding kinematic inversions and previous general knowledge of rupture dynamics. Machine learning might provide a great tool for the assimilation, e.g., to filter out models that would lead to clearly too small or too large ruptures.

Any effort to decrease the computational requirements of the physics-based source inversions may promote their further spread. Dynamic inversions then have the potential to substitute the kinematic inversions and become a routine tool for studies of larger earthquakes. Although the recent dynamic inversions were only performed with the relatively simple dynamic source model, the Bayesian methodology is suitable for incorporating more advanced physics-based models, encompassing a wider range of fault phenomena than coseismic slip. In the future, more physically-complex models in combination with the available decades of GPS measurements and thousands of years of information about historical earthquakes could then lead to inverse modeling of the long-term seismic cycle models and pave the way to understanding the full spatially-temporal scale of the fault processes.

Bibliography

J. P. Ampuero and Y. Ben-Zion. Cracks, pulses and macroscopic asymmetry of dynamic rupture on a bimaterial interface with velocity weakening friction. *Geophys. J. Int.*, 173(2):674–692, 2008.

R. Ando and Y. Kaneko. Dynamic rupture simulation reproduces spontaneous multifault rupture and arrest during the 2016 M w 7.9 Kaikoura earthquake. *Geophys. Res. Lett.*, 45:12875–12883, 2018.

D. J. Andrews. Rupture velocity of plane strain shear cracks. *J. Geophys. Res.*, 81(32):5679– 5687, 1976.

K. Bai and J.-P. Ampuero. Effect of seismogenic depth and background stress on physical limits of earthquake rupture across fault step overs. *J. Geophys. Res.: Solid Earth*, 122:10280–10298, 2017.

M. Barall. A grid-doubling finite-element technique for calculating dynamic three-dimensional spontaneous rupture on an earthquake fault. *Geophys. J. Int.*, 178 (2):845–859, 2006.

M. Barall and R. A. Harris. Metrics for comparing dynamic earthquake rupture simulations. *Seismol. Res. Lett.*, 86(1):223–235, 2015.

W. Barnhart, J. Murray, S.-H. Yun, J. Svarc, S. Samsonov, E. Fielding, B. Brooks, and P. Milillo. Geodetic constraints on the 2014 Mw 6.0 South Napa earthquake. *Seism. Res. Lett.*, 86:335–343, 2015.

N. Beeler, T. Tullis, and D. Goldsby. Constitutive relationships and physical basis of fault strength due to flash heating. *J. Geophys. Res.*, 113:B01401, 2008.

W. F. Brace and J. D. Byerlee. Stick slip as a mechanism for earthquakes. *Science*, 153:990–992, 1966.

B. A. Brooks, S. E. Minson, C. L. Glennie, J. M. Nevitt, T. Dawson, and R. Rubin. Buried shallow fault slip from the South Napa earthquake revealed by near-field geodesy. *Sci. Adv.*, 3(7):e1700525, 2017.

S. Bunichiro, H. Noda, and M. J. Ikari. Quasi-Dynamic 3D Modeling of the Generation and Afterslip of a Tohoku-oki Earthquake Considering Thermal Pressurization and Frictional Properties of the Shallow Plate Boundary. *Pure and Applied Geophysics*, 176:3951–3973, 2019.

R. Burridge. The numerical solution of certain integral equations with non-integrable kernels arising in the theory of crack propagation and elastic wave diffraction. *Phil. Trans. Roy. Soc. Lond.*, 265:353–381, 1969.

F. Collino and Ch. Tsogka. Application of the perfectly matched absorbing layer model to the linear elastodynamic problem in anisotropic heterogeneous media. *Geophysics*, 66:294–307, 2001.

F. Cotton and O. Coutant. Dynamic stress variations due to shear faults in a plane-layered medium. *Geophys. J. Int.*, 128:676–688, 1997.

P. A. Cowie and C. H. Scholz. Growth of faults by the accumulation of seismic slip. *J. Geophys. Res.*, 97:11085–11095, 1992.

V. M. Cruz-Atienza, J. Virieux, and H. Aochi. 3D finite-difference dynamic-rupture modeling along nonplanar faults. *Geophysics*, 72(5):123–137, 2007.

T. M. Daley, B. M. Freifeld, J. Ajo-Franklin, S. Dou, R. Pevzner, V. Shulakova, et al. Field Testing of Fiber-Optic Distributed Acoustic Sensing (DAS) for Subsurface Seismic Monitoring. *Lead. Edge*, 32(6):699–706, 2013.

L. A. Dalguer and S. M. Day. Staggered-grid split-node method for spontaneous rupture simulation. *J. Geophys. Res.*, 112:B02302, 2007.

S. M. Day, L. A. Dalguer, N. Lapusta, and Y. Liu. Comparison of finite difference and boundary integral solutions to three-dimensional spontaneous rupture. *J. Geophys. Res.*, 110:B12307, 2005.

J. de la Puente, J.-P. Ampuero, and M. Käser. Dynamic rupture modeling on unstructured meshes using a discontinuous Galerkin method. *J. Geophys. Res.*, 114:B10302, 2009.

S. B. DeLong, A. Donnellan, D. J. Ponti, R. S. Rubin, J. J. Lienkaemper, C. S. Prentice, T. E. Dawson, G. Seitz, D. P. Schwartz, K. W. Hudnut, C. Rosa, A. Pickering, and J. W. Parker. Tearing the terroir: Details and implications of surface rupture and deformation from the 24 August 2014 M6.0 South Napa earthquake, California. *Earth Space Sci.*, 3:416–430, 2016.

G. Di Toro, D. L. Goldsby, and T. E. Tullis. Friction falls towards zero in quartz rock as slip velocity approaches seismic rates. *Nature*, 427:436–439, 2004.

J. H. Dieterich. Time-dependent friction as a possible mechanism for aftershocks. *J. Geophys. Res.*, 77(20):3771–3781, 1972.

J. H. Dieterich. Modeling of rock friction: 1. experimental results and constitutive equations. *J. Geophys. Res.*, 84(B5):2161– 2168, 1979.

D. S. Dreger, M.-H. Huang, A. Rodgers, T. Taira, and K. Wooddell. Kinematic finite-sourcemodel for the 24 August 2014 South Napa, California, earthquake from joint inversionof seismic, GPS, and InSAR data. *Seismol. Res. Lett.*, 86: 327–334, 2015.

E. M. Dunham, D. Belanger, L. Cong, and J. E. Kozdon. Earthquake ruptures with strongly rate-weakening friction and off-fault plasticity, part 1: Planar faults. *Bull. Seismol. Soc. Am.*, 101:2296–2307, 2011.

M. A. Floyd, R. J. Walters, J. R. Elliott, G. J. Funning, J. L. Svarc, J. R. Murray, A. J. Hooper, Y. Larsen, P. Marinkovic, R. Bürgmann, I. A. Johanson, and T. J. Wright. Spatial variations in fault friction related to lithology from rupture and afterslip of the 2014 South Napa, California, earthquake. *Geophys. Res. Lett.*, 43(13):6808–6816, 2016.

C. Frohlich. *Deep Earthquakes*. Cambridge University Press, 2006.

J. I. Fukuda, K. M. Johnson, K. M. Larson, and S. I. Miyazaki. Fault friction parameters inferred from the early stages of afterslip following the 2003 Tokachi-oki earthquake. *J. Geophys.Res. Solid Earth*, 114:B04412, 2009.

E. Fukuyama and T. Mikumo. Dynamic rupture analysis: Inversion for the source process of the 1990 Izu-Oshima, Japan, earthquake. *J. Geophys. Res.*, 98:6529–6542, 1993.

P. M. Fulton, E. Brodsky, J. J. Mori, and F. M. Chester. Tohoku-Oki Fault Zone Frictional Heat Measured During IODP Expeditions 343 and 343T. *Oceanography*, 32:102–104, 2019.

A.-A. Gabriel, J.-P. Ampuero, L. A. Dalguer, and P. M. Mai. The transition of dynamic rupture styles in elastic media under velocity-weakening friction. *J. Geophys. Res.*, 117:B09311, 2012.

F. Gallovič. Heterogeneous Coulomb stress perturbation during earthquake cycles in a 3D rate-and-state fault model. *Geophys. Res. Lett.*, 35:L21306, 2008.

F. Gallovič, L. Valentová, J.-P. Ampuero, and A.-A. Gabriel. Bayesian dynamic finite-fault inversion: 1. Method and synthetic test. *J. Geophys. Res.*, 124: 6949–6969, 2019a.

F. Gallovič, L. Valentová, J.-P. Ampuero, and A.-A. Gabriel. Bayesian dynamic finite-fault inversion: 2. Application to the 2016 Mw 6.2 Amatrice, Italy, earthquake. *J. Geophys. Res.*, 124:6970–6988, 2019b.

F. Gallovič, J. Zahradník, V. Plicka, E. Sokos, C. Evangelidis, I. Fountoulakis, and F. Turhan. Complex rupture dynamics on an immature fault during the 2020 Mw 6.8 Elazığ earthquake, Turkey. *Commun. Earth Environ.*, 1:40, 2020.

P. Galvez, A. Petukhin, P. Somerville, J. P. Ampuero, K. Miyakoshi, D. Peter, and K. Irikura. Multicycle simulation of strike-slip earthquake rupture for use in near-source ground-motion simulations. *Bull. Seismol. Soc. Am.*, 111: 2463–2485, 2021.

R. W. Graves. Simulating seismic wave propagation in 3D elastic media using staggered-grid finite differences. *Bull. Seismol. Soc. Am.*, 86(4):1091–1106, 1996.

R. W. Graymer, D. A. Ponce, R. C. Jachens, R. W. Simpson, G. A. Phelps, and C. M. Wentworth. Three-dimensional geologic map of the Hayward fault, northern California: Correlation of rock units with variations in seismicity, creep rate, and fault dip. *Geology*, 33:521–524, 2005.

R. W. Graymer, B. C. Moring, G. J. Saucedo, C. M. Wentworth, E. E. Brabb, and K. L. Knudsen. Geologic map of the San Francisco Bay region. Technical report, U.S. Geological Survey, Scientific Investigations Map 2918, 2006. URL `http://pubs.usgs.gov/sim/2006/2918/`.

J. L. Hardebeck and D. R. Shelly. Aftershocks of the 2014 South Napa, California, earthquake:Complex faulting on secondary faults. *Bull. Seismol. Soc. Am.*, 106: 1100–1109, 2016.

R. Harris, M. Barall, R. Archuleta, E. Dunham, B. T. Aagaard, Jean Paul Ampuero, H. Bhat, V. Cruz-Atienza, L. Dalguer, P. Dawson, S. Day, Duan , G. Ely, Y. Kaneko, Y. Kase, N. Lapusta, Y. Liu, S. Ma, D. Oglesby, and E. Templeton. The SCEC/USGS dynamic earthquake rupture code verification exercise. *Seismol. Res. Lett.*, 80(1):119–126, 2009.

R. A. Harris. Large earthquakes and creeping faults. *Rev. Geophys.*, 55:169–198, 2017.

R. A. Harris, M. Barall, D. J. Andrews, B. Duan, S. Ma, E. M. Dunham, A.-A. Gabriel, Y. Kaneko, Y. Kase, B. T. Aagaard, et al. Verifying a computational method for predicting extreme ground motion. *Seismol. Res. Lett.*, 82 (5):638–644, 2011.

R. A. Harris, M. Barall, B. Aagaard, S. Ma, D. Roten, K. Olsen, B. Duan, D. Liu, B. Luo, K. Bai, et al. A suite of exercises for verifying dynamic earthquake rupture codes. *Seismol. Res. Lett.*, 89(3):1146–1162, 2018.

A. Heinecke, A. Breuer, S. Rettenberger, M. Bader, A.-A. Gabriel, C. Pelties, A. Bode, W. Barth, X.-K. Liao, K. Vaidyanathan, et al. Petascale high order dynamic rupture earthquake simulations on heterogeneous supercomputers. In *Proc. of the International Conference for High Performance Computing, Networking, Storage and Analysis SC14*, New Orleans, Louisiana, 2014.

G. Hillers, Y. Ben-Zion, and P. M. Mai. Seismicity on a fault controlled by rate- and state-dependent friction with spatial variations of the critical slip distance. *J. Geophys. Res.: Solid Earth*, 111:B01403, 2006.

Y. Ida. Cohesive force across the tip of a longitudinal-shear crack and Griffith's specific surface energy. *J. Geophys. Res.*, 77(20):3796–3805, 1972.

C. Ji, R. J. Archuleta, and C. Twardzik. Rupture history of 2014 Mw 6.0 South Napa earthquakeinferred from near-fault strong motion data and its impact to the practice of ground strong motion prediction. *Geophys. Res. Lett.*, 42: 2149–2156, 2015.

Y. Kaneko, N. Lapusta, and J.-P. Ampuero. Spectral-element modeling of spontaneous earthquake rupture on rate and state faults: Effect of velocity-strengthening friction at shallow depths. *J. Geophys. Res.*, 113:B0931, 2008.

D. Komatitsch, D. Michea, and G. Erlebacher. Porting a high-order finite-element earthquake modeling application to nvidia graphic cards using cuda. *J. Parallel Distr. Comput.*, 69(5):451–460, 2009.

D. Komatitsch, P. Le Loher, D. Michéa, G. Erlebacher, and D. Göddeke. Accelerating spectral-element and finite-difference wave propagation algorithms using a cluster of GPU graphics cards. In *Workshop Défis Actuels De La Modélisation Électromagnétique: Gestion De La Complexité, Multi-Échelle, Multi-Physique, Gestion Des Incertitudes, Statistiques*, Saint Malo, France, 2010. in French.

F. Kostka, J. Zahradník, E. Sokos, and F. Gallovič. Assessing the role of selected constraintsin Bayesian dynamic source inversion: Application to the 2017 Mw 6.3 Lesvos earthquake. *Geophys. J. Int.*, 228:711–727, 2022.

J. Langbein, J. R. Murray, and H. A. Snyder. Coseismic and initial postseismic deformationfrom the 2004 Parkfield, California, earthquake, observed by Global Positioning System,electronic distance meter, creepmeters, and borehole strainmeters. *Bull. Seismol. Soc. Am.*, 96:S304–S320, 2006.

R. Langenheim, R. Graymer, R. Jachens, and D. Mclaughlin. Geophysical framework of the northern san francisco bay region, california. *Geosphere*, 6:594–620, 2010.

N. Lapusta, J. R. Rice, Y. Ben-Zion, and G. Zheng. Elastodynamic analysis for slow tectonic loading with spontaneous rupture episodes on faults with rate- and state-dependent friction. *J. Geophys. Res.*, 105:23765–23789, 2000.

N. Lapusta et al. Modeling earthquake source processes: from tectonics to dynamic rupture. Technical report, National Science Foundation (NSF), Southern California Science Center (SCEC),Seismological Laboratory at the California Institute of Technology, 2019.

A. Levander. Fourth-order finite-difference P-SV seismograms. *Geophysics*, 53: 1425–1436, 1988.

J. J. Lienkaemper, S. B. DeLong, C. J. Domrose, and C. M. Rosa. Afterslip behavior following the 2014 M 6.0 South Napa earthquake with implications for afterslip forecastingon other seismogenic faults. *Seism. Res. Lett.*, 87:609–619, 2016.

R. B. Lohman, M. Simons, and B. Savage. Location and mechanism of the Little Skull Mountain earthquake as constrained by satellite radar interferometry and seismic waveform modeling. *J. Geophys. Res.*, 107:B6, 2002.

R. Madariaga. Dynamics of an expanding circular fault. *Bull. Seismol. Soc. Am.*, 66:639–666, 1976.

R. Madariaga, K. Olsen, and R. Archuleta. Modeling dynamic rupture in a 3D earthquake fault model. *Bull. Seismol. Soc. Am.*, 88(5):1182–1197, 1998.

Ch. Marone, C. Scholz, and R. Bilham. On the mechanics of earthquake afterslip. *J. Geophys. Res.*, 96:8441–8452, 1991.

F. S. McFarland, J. J. Lienkaemper, and S. J. Caskey. Data from theodolite measurements of creep rates on San Francisco Bay Region faults, California: 1979–2013. Technical report, U.S. Geological Survey Open-File Report 2009, 2015.

D. Melgar, J. Geng, B. W. Crowell, J. S. Haase, Y. Bock, W. C. Hammond, and R. M. Allen. Seismogeodesy of the 2014 Mw6. 1 Napa earthquake, California: Rapid responseand modeling of fast rupture on a dipping strike-slip fault. *J. Geophys. Res.: Solid Earth*, 120:5013–5033, 2015.

D. Michéa and D. Komatitsch. Accelerating a three-dimensional finite-difference wave propagation code using GPU graphics cards. *Geophys. J. Int.*, 182: 389–402, 2010.

Y. Okada. Surface deformation due to shear and tensile faults in a half-space. *Bull. Seism.Soc. Am.*, 75:1135–1154, 1985.

K. Okubo, H. S. Bhat, E. Rougier, S. Marty, A. Schubnel, Z. Lei, E. E. Knight, and Y. Klinger. Dynamics, radiation, and overall energy budget of earthquake rupture with coseismic off-fault damage. *J. Geophys. Res.: Solid Earth*, 124: 11771–11801, 2019.

C. Pelties, J. De la Puente, J.-P. Ampuero, G. B. Brietzke, and M. Käser. Three-dimensional dynamic rupture simulation with a high-order discontinuous Galerkin method on unstructured tetra-hedral meshes. *J. Geophys. Res.*, 117:B02309, 2012.

C. Pelties, A.-A. Gabriel, and J.-P. Ampuero. Verification of an ADER-DG method for complex dynamic rupture problems. *Geosci. Model Dev.*, 7(3): 847–866, 2014.

H. Perfettini and J.-P. Ampuero. Dynamics of a velocity strengthening fault region: Implications for slow earthquakes and postseismic slip. *J. Geophys. Res.*, 113:B09411, 2008.

H. Perfettini and J.-P. Avouac. Postseismic relaxation driven by brittle creep: A possible mechanism to reconcile geodetic measurements and the decay rate of aftershocks,application to the Chi-Chi earthquake, Taiwan. *J. Geophys. Res.*, 109:B02304, 2004.

H. Perfettini and J. P. Avouac. The seismic cycle in the area of the 2011 Mw9.0 Tohoku-Oki earthquake. *Journ. Geophys. Res.: Solid Earth*, 119(5):4469–4515, 2014.

H. Perfettini, J. Schmittbuhl, and A. Cochard. Shear and normal load perturbations on a two-dimensional continuous fault: 1. Static triggering. *J. Geophys. Res.*, 108:2408, 2003.

S. Peyrat, K. Olsen, and R. Madariaga. Dynamic modeling of the 1992 Landers earthquake. *J. Geophys. Res.*, 193:1691–1712, 2001.

A. Pitarka. Rupture dynamics simulations of shallow crustal earthquakes on reverse slip faults. Technical report, Lawrence Livermore National Laboratory, 2020.

J. Premus, F. Gallovič, L. Hanyk, and A.-A. Gabriel. FD3D_TSN: A fast and simple code for dynamic rupture simulations with GPU acceleration. *Seism. Res. Lett.*, 91:2881–2889, 2020.

J. Premus, F. Gallovič, and J.-P. Ampuero. Bridging time scales of faulting: From coseismic to postseismic slip of the Mw 6.0 2014 South Napa, California earthquake. *Sci. Adv.*, 8:eabq2536, 2022.

J. R. Rice. Spatio-temporal complexity of slip on a fault. *J. Geophys. Res.*, 98: 9885–9907, 1993.

J. R. Rice. Heating and weakening of faults during earthquake slip. *J. Geophys. Res.: Solid Earth*, 111:B05311, 2006.

J. R. Rice and Y. Ben-Zion. Slip complexity in earthquake fault models. *Proc. Natl. Acad. Sci. U.S.A.*, 93:3811–3818, 1996.

A. J. Rodgers, R. Pankajakshan, B. Sjogreen, A. Petersson, and A. Pitarka. Hayward fault earthquake ground motion simulations on GPU-accelerated platforms with SW4-RAJA. In *Presentation at 2019 SCEC Annual Meeting*, Palm Springs, California, 2019.

D. Roten, K. B. Olsen, S. M. Day, Y. Cui, and D. Fäh. Expected seismic shaking in los angeles reduced by san andreas fault zone plasticity. *Geophys. Res. Lett.*, 41:2769–2777, 2014.

A. Ruina. Slip instability and state variable friction laws. *J. Geophys. Res.*, 881: 10359– 10370, 1983.

M. Sambridge. A parallel tempering algorithm for probabilistic sampling and multimodal optimization. *Geophys. J. Int.*, 196:357–374, 2013.

C. Scholz. Earthquakes and friction laws. *Nature*, 391:37–42, 1998.

C. Scholz. *The Mechanics of Earthquakes and Faulting*. Cambridge Univ. Press„ 2. edition, 2012.

D. Storchak, J. Harris, L. Brown, K. Lieser, B. Shumba, and D. Di Giacomo. Rebuild of the Bulletin of the International Seismological Centre (ISC)—part 2: 1980–2010. *Geosci. Lett.*, 7, 2020.

E. Tinti, E. Casarotti, T. Ulrich, T. Taufiqurrahman, D. Li, and A.-A. Gabriel. Constraining families of dynamic models using geological, geodetic and strong ground motion data: The Mw 6.5, October 30th, 2016, Norcia earthquake, Italy. *Earth Planet. Sci Lett.*, 576:117237, 2021.

C. Twardzik, M. Vergnolle, A. Sladen, and L. L. Tsang. Very early identification of a bimodal frictional behavior during the post-seismic phase of the 2015 Mw 8.3 Illapel, Chile, earthquake. *Solid Earth*, 12:2523–2537, 2021.

T. Ulrich, A.-A. Gabriel, J.-P. Ampuero, and W. Xu. Dynamic viability of the 2016 Mw 7.8 Kaikuoura earthquake cascade on weak crustal faults. *Nat. Comm.*, 10:1213, 2019.

C. Uphoff, S. Rettenberger, M. Bader, E. Madden, T. Ulrich, S. Wollherr, and A.-A. Gabriel. Extreme scale multi-physics simulations of the tsunamigenic 2004 Sumatra megathrust earthquake. In *SC '17: Proc. of the International Conference for High Performance Computing, Networking, Storage and Analysis*, Denver, Colorado, 2017.

R. Viesca and D. Garagash. Ubiquitous weakening of faults due to thermal pressurization. *Nat. Geosci.*, 8:875–879, 2015.

S. Wei, S. Barbot, R. Graves, J. J. Lienkaemper, T. Wang, K. Hudnut, Y. Fu, and D. Helmberger. The 2014 Mw 6.1 South Napa Earthquake: A unilateral rupture with shallow asperityand rapid afterslip. *Seism. Res. Lett.*, 86:344–354, 2015.

J. R. Wesling and K. L. Hanson. Mapping of the West Napa Fault Zone for input into the northern California Quaternary fault database. Technical report, U.S. Geological Survey Open File Report 05HQAG0002, 2008.

T. Yamashita. Generation of microcracks by dynamic shear rupture and its effects on rupture growth and elastic wave radiation. *Geophys. J. Int.*, 143(2):395–406, 2000.

J. Zhou, Y. Cui, E. Poyraz, D. J. Choi, and C. C. Guest. Multi-GPU implementation of a 3D finite difference time domain earthquake code on heterogeneous supercomputers. *Procedia Comput. Sci.*, 18:1255–1264, 2013.

List of publications

1. [Premus et al., 2020]: J. Premus, F. Gallovič, L. Hanyk, and A.-A. Gabriel. FD3D_TSN: A fast and simple code for dynamic rupture simulations with GPU acceleration. *Seism. Res. Lett.*, 1:2881–2889, 2020.

2. [Premus et al., 2022]: J. Premus, F. Gallovič, and J.-P. Ampuero. Bridging time scales of faulting: From coseismic to postseismic slip of the Mw 6.0 2014 South Napa, California earthquake. *Sci. Adv.*, 8:eabq2536, 2022.